

# Electron interactions in an antidot in the integer quantum Hall regime

H.-S. Sim \*

*Department of Physics, Korea Advanced Institute of Science and Technology,  
373-1 Guseong-dong, Yuseong-gu, Daejeon 305-701, Korea*

M. Kataoka and C. J. B. Ford

*Cavendish Laboratory, J J Thomson Avenue, Cambridge CB3 0HE, United  
Kingdom*

---

## Abstract

A quantum antidot, a submicron depletion region in a two-dimensional electron system, has been actively studied in the past two decades, providing a powerful tool for understanding quantum Hall systems. In a perpendicular magnetic field, electrons form bound states around the antidot. Aharonov-Bohm resonances through such bound states have been experimentally studied, showing interesting phenomena such as Coulomb charging,  $h/2e$  oscillations, spectator modes, signatures of electron interactions in the line shape, Kondo effect, etc. None of them can be explained by a simple noninteracting electron approach. Theoretical models for the above observations have been developed recently, such as a capacitive-interaction model for explaining the  $h/2e$  oscillations and the Kondo effect, numerical prediction of a hole maximum-density-droplet antidot ground state, and spin density-functional theory for investigating the compressibility of antidot edges. In this review, we summarize such experimental and theoretical works on electron interactions in antidots.

*Key words:* Antidot, Quantum Hall effects, Edge states, Aharonov-Bohm effect, Electron-electron interactions, Electron transport, Mesoscopic systems

*PACS:* 73.43.-f, 73.23.Hk, 73.23.-b, 72.15.Qm

---

## Contents

1	Introduction	3
2	Noninteracting description of an integer quantum Hall antidot	7
2.1	Single-particle energy levels	7
2.2	Aharonov-Bohm oscillations	10
3	Experimental signatures of electron interactions in antidots	15
3.1	Typical experimental setup	16
3.2	Simple Aharonov-Bohm oscillations	18
3.3	Detection of antidot charging	22
3.4	$h/2e$ Aharonov-Bohm oscillations	26
3.5	Spectator modes in antidot molecules	30
3.6	Line shape of Aharonov-Bohm resonances	33
3.7	Compressible regions around antidots	35
3.8	Kondo-like zero-bias anomaly	40
4	Theoretical studies on electron interactions in antidots	43
4.1	Total Hamiltonian	44
4.2	Derivation of excess charge	45
4.3	Capacitive interaction model for $\nu_c = 2$ antidots	50
4.4	Antidot Kondo effect	55
4.5	Hole maximum-density-droplet antidot ground state	58

---

\* Corresponding author.  
*Email address:* `hssim@kaist.ac.kr` ( H.-S. Sim ).

4.6	Density-functional studies on the compressibility of antidot states	62
5	Summary and perspectives	64
	References	67

## 1 Introduction

An antidot is a potential hill in a two-dimensional electron gas (2DEG) formed in a GaAs/AlGaAs heterostructure. It can be created by a negative voltage on a surface gate (for example, see Refs. [1,2]) or by an etched pit in the wafer surface (Refs. [3,4]). It is often regarded as an artificial repulsive impurity and thus considered to be the counterpart of a quantum dot [5,6]. The idea of an antidot in a quantum Hall system was first introduced by Jain and Kivelson [7] in order to explain resistance peaks observed in a narrow Hall bar [8]. The first experimental observation of Aharonov-Bohm oscillations in a gate-controllable antidot was made by Smith and his coworkers in 1989 [9].

By applying magnetic fields perpendicular to the 2DEG, antidots have been extensively and intensively investigated to understand coherent electron scattering, localized antidot states, the quantum Hall effect, and many-body interaction effects. In the regime of weak magnetic fields, an antidot behaves as a simple scattering center. In this regime, antidot superlattices provide a good tool for studying semiclassical motion of electrons under periodic scattering centers, for example, commensurate Weiss oscillations [10,11,12] and chaotic motions [13,14]. On the other hand, under strong magnetic fields of the order of a Tesla, an antidot provides a local depletion region inside quantum Hall systems [15]. In this regime, quantum Hall edge states [16] can form closed chiral orbits around the antidot (see Fig. 1). The localized orbits around a single antidot [1,2,17,18,19,20,21,22,23,24,25,26] and around an antidot molecule [27,28,29] have been studied in the integer quantum Hall regime by measuring Aharonov-Bohm oscillations of conductance, which occur when the localized orbits couple to extended edge channels along the boundary of the 2DEG. The antidot has also been investigated in the fractional quantum Hall regime experimentally [4,11,30,31,32,33,34,35] and theoretically [36,37,38,39,40,41] to understand quasiparticle tunneling, charge and statistics, composite fermions, chiral Luttinger liquids, and non-Abelian statistics of the fractional quantum Hall  $5/2$  state.

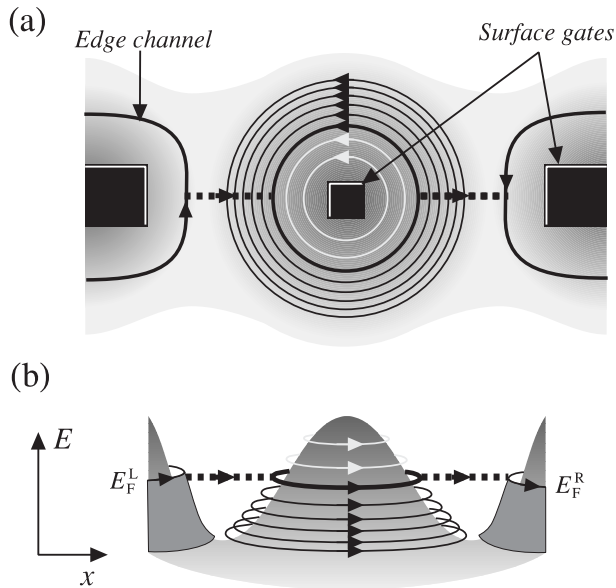


Fig. 1. Single-particle states formed around an antidot in the integer quantum Hall regime (ignoring self-consistent effects). (a) Top view: The antidot potential is created by the voltage applied on the central surface gate, while the constriction width between the antidot states and the extended quantum Hall edge channels can be controlled by tuning the side gates. The central and side surface gates are shown as filled boxes. Filled and empty single-particle states encircling the antidot are shown in black and light-grey lines, respectively. The dotted lines represent the tunneling between the antidot state (shown as bold) and the extended edge channels along the left and right edges (with the Fermi levels  $E_F^L$  and  $E_F^R$ , respectively). (b) Side view: the potential profile created by the voltages on the antidot and side gates, depicting the continuum of states along the extended edges, and the discrete states around the antidot.

In a simple description of the integer quantum Hall effect, electron-electron interactions are often neglected. Thus, one might expect that single-particle localized edge states are enough to describe the antidot states in the integer quantum Hall regime. However, contrary to this naive expectation, there has recently been a series of interesting experimental observations in the regimes of antidot local filling factor one or two, which include  $h/2e$  Aharonov-Bohm conductance oscillations [1,2,23,26], the signature of electron interactions shown in the line shape of conductance peaks [21], the detection of antidot charging effect [22], Kondo effect [25], and spectator modes in

an antidot molecule [28]. None of these observations can be understood within single-particle models [18,20,42,43]. Note that the importance of Coulomb interactions has also been reported in other experimental works on integer quantum Hall systems such as in scanning probe studies of quantum Hall localized states [44,45,46] and in the realization of electronic quantum Hall Mach-Zehnder interferometers [47,48].

The starting point of understanding such experimental observations in the integer quantum Hall antidots is *excess charge* [1]. The excess charge can be formed around an antidot due to the magnetic flux quantization. When the magnetic field  $B$  (perpendicular to the surface of the sample) changes adiabatically, each single-particle state encircling the antidot moves with respect to the antidot potential, adjusting the enclosed area  $S$  in order to keep the flux  $BS$  constant (see Sec. 4.2 for details). The phase change of the wavefunction around the antidot increases by  $2\pi$  for each unit of flux  $h/e$  enclosed, through the Aharonov-Bohm effect. If the occupation of these states does not change, the electron displacement results in a local charge imbalance around the antidot, i.e., local accumulation of excess charges. Excess charges can provide a source of electron-electron interactions in the antidot.

Recently, a phenomenological model for integer quantum Hall antidots has been proposed [49] to describe the capacitive interaction of excess charges. This model provides a good explanation of the experimental observations of the  $h/2e$  Aharonov-Bohm oscillations, the antidot charging effect, and the antidot Kondo effect, indicating that the capacitive interaction of excess charges is a good starting point for understanding electron interactions in antidots. The model is reminiscent of the constant-interaction model for quantum dots [5,6,50]. To see the microscopic nature of electron interactions and of many-body antidot states, numerical Hartree-Fock calculations have been performed [51,52,53]. It has been found [52] that the Hartree-Fock results for a large antidot can be well described by the capacitive interaction model.

The formation of compressible regions around an antidot is also an interesting issue. In the quantum Hall regime, there is no charge screening in incompressible bulk regions because of the quantum Hall energy gap at the Fermi level, while screening effects are important along compressible extended edge regions [54,55] where the local filling factor decreases from the bulk value to zero. The combined effects of the energy gap and the screening result in the formation of alternate compressible and incompressible strips along the extended edge regions of the 2DEG. The widths of the compressible strips can be determined in a self-consistent treatment of Coulomb interactions [56,57]. On the other hand, an antidot provides a closed finite edge of a

quantum Hall system. Due to finite-size effects (discrete energy levels), the properties of the compressible regions formed around an antidot are expected to deviate from those formed along the extended edge regions, as the antidot size decreases. There has been controversy [23,24,58,59,61] about whether compressible regions can be formed around a small-size antidot, or in what range of fields. Recent numerical work on an antidot, based on spin density functional theory, has shown [60] that compressible regions around an antidot can be narrower than those along the extended edges because of weaker screening effects. It was also shown that exchange interactions play an important role in determining the width of compressible regions around an antidot.

In this article, we review recent experimental and theoretical works devoted to electron interactions in antidots in the integer quantum Hall regime. In the experimental parts, we describe the direct evidence of the antidot charging effect [22], the  $h/2e$  Aharonov-Bohm oscillations of conductance [1,2,23,26], the spectator mode in an antidot molecule [28], the signature of electron interactions shown in the line shape of Aharonov-Bohm peaks [21], the experimental search for compressible regions [23,24,58,59,61], and the antidot Kondo effect [25]. In the theoretical parts, we explain the origin of excess charges on an antidot and introduce the capacitive interaction of excess charges, which may give rise to the antidot charging effect. Then, we show that the capacitive interaction model can give a good explanation [49] for the  $h/2e$  oscillations and the antidot Kondo effect. We also include the prediction [52] of a hole maximum-density droplet of antidot states based on a numerical Hartree-Fock approach and the numerical spin density-functional search for compressible regions of an antidot [60]. Despite the above experimental and theoretical efforts, there are still many open problems in antidots in the integer quantum Hall regime. We suggest some possible open questions in the concluding part of the review. We note that antidots in the fractional quantum Hall regime are not addressed in this review.

This paper is organized as follows. In Sec. 2, the single-particle description of an integer quantum Hall antidot is briefly introduced. Single-particle energy levels (Sec. 2.1), forward and backward scattering of extended edge channels by antidots, a noninteracting electron description of the Aharonov-Bohm oscillations, and the two-terminal conductance of an antidot (Sec. 2.2) are discussed. In Sec. 3, experimental works on electron interactions are mentioned. This section includes typical experimental setups (Sec. 3.1) and experimental data (Sec. 3.2), the detection of the antidot charging effect (Sec. 3.3), the  $h/2e$  Aharonov-Bohm oscillations (Sec. 3.4), the spectator modes in an antidot molecule (Sec. 3.5), the line shape of Aharonov-Bohm peaks (Sec. 3.6), the search for compressible regions around an antidot (Sec. 3.7), and the antidot

Kondo effect (Sec. 3.8). In Sec. 4, we describe theoretical models dealing with electron interactions in an antidot. This section provides the total Hamiltonian of an antidot system (Sec. 4.1), the origin of excess charges (Sec. 4.2), the capacitive interaction model for an antidot (Sec. 4.3), the explanation of the  $h/2e$  oscillations and the antidot Kondo effect (Sec. 4.4), the prediction of a hole maximum-density-droplet antidot ground state (Sec. 4.5), and the numerical search for compressible regions (Sec. 4.6). Finally, open problems and perspectives of the integer quantum Hall antidot research will be given in Sec. 5.

## 2 Noninteracting description of an integer quantum Hall antidot

In this section, we sketch a single-particle model of an integer quantum Hall antidot. In Sec. 2.1, we describe single-particle localized states around an isolated antidot. The properties of the single-particle states are governed by the Aharonov-Bohm flux enclosed by them. In Sec. 2.2, we discuss resonant scattering when electrons can tunnel between the extended edges of the 2DEG and the antidot. The resonant scattering can result in the flux-dependent Aharonov-Bohm oscillations of conductance, the line shape of which depends on the detailed coupling nature of the antidot to the extended edge channels.

### 2.1 Single-particle energy levels

We first consider an isolated antidot where the antidot states are decoupled from the extended edge channels of the 2DEG. In a magnetic field  $B$  perpendicular to the 2DEG, classical skipping orbits appear around the antidot due to  $\vec{E} \times \vec{B}$  drift with electric field  $\vec{E}$  created by the antidot potential. The skipping orbits are quantized (see Fig. 1) so that their enclosing area  $S_m$  satisfies the Aharonov-Bohm condition

$$BS_m \sim m\phi_0, \tag{1}$$

where  $m$  is the orbital quantum number,  $\phi_0 = h/e$  is the magnetic flux quantum,  $h$  is Planck's constant, and  $e$  is the magnitude of the electronic charge. Due to the sloping shape of the antidot potential, the quantized states form a ladder in energy around the antidot [Fig. 1(b)]. At zero temperature these states are filled up to the Fermi

level  $E_F$  when electron-electron interactions are neglected. For simplicity, hereafter, we assume that the antidot orbits have a circular shape.

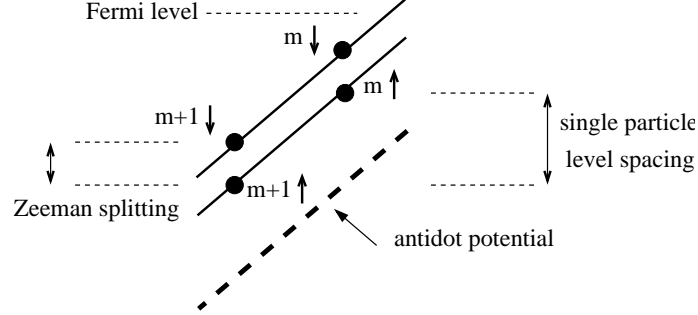


Fig. 2. Schematic energy diagram of single-particle antidot states. For simplicity, only the spin-split branches of the lowest Landau level are drawn. The single-particle energy spacing  $\delta\epsilon_m$  between the  $m$ -th and  $(m + 1)$ -th localized states and Zeeman energy splitting of spin-up (up arrows) and down (down arrows) states are shown. Spin-up states are assumed to have smaller Zeeman energy than spin-down states. The dashed line indicates the antidot potential.

The properties of the single-particle antidot states can be understood from the Landau levels. Using the symmetric gauge, one can have, for example, the  $m$ -th orbital state  $\phi_m$  in the lowest Landau level [15],

$$\phi_m(\vec{r}) = \frac{1}{\sqrt{2^m \pi (m-1)! l_B}} \left(\frac{z}{l_B}\right)^{m-1} \exp\left(\frac{-|z|^2}{4l_B^2}\right), \quad (2)$$

where  $z = x + iy$  is the complex coordinate of the two-dimensional plane,  $m \geq 1$  is the orbital quantum number used above, and  $l_B = \sqrt{\hbar/(eB)} = 25.6/\sqrt{B[\text{T}]}[\text{nm}]$  is the magnetic length. The state  $\phi_m$  encloses  $m$  units  $h/e$  of magnetic flux, *i.e.*, the magnetic flux enclosed within  $r_m$  (given by  $r_m^2 \equiv \langle \phi_m | r^2 | \phi_m \rangle = 2ml_B^2$ ) is quantized. The state is confined radially within the magnetic length scale  $l_B$  due to the perpendicular magnetic field. In the presence of the antidot potential  $V_{\text{AD}}(r)$ , when  $V_{\text{AD}}(r)$  varies sufficiently slowly on the scale of  $l_B$ , one can use the states  $\phi_m$  as the single-particle states of the isolated antidot with single-particle energy  $\epsilon_m$ ,

$$\epsilon_{m\sigma} \simeq \frac{1}{2}\hbar\omega_c + \bar{V}_{\text{AD}}(m) + \epsilon_{\sigma}^Z, \quad (3)$$



where  $\omega_c = eB/m^*$  is the cyclotron frequency,  $m^*$  is the electron effective mass ( $m^* = 0.067m_e$  for GaAs),  $\bar{V}_{\text{AD}}(m) = \langle \phi_m | V_{\text{AD}} | \phi_m \rangle$  is the mean antidot potential energy,  $\epsilon_\sigma^Z = g\mu_B B\sigma/2$  is the Zeeman energy of a spin- $\sigma$  electron,  $\mu_B$  is the Boltzmann factor,  $g$  is the Landé  $g$  factor ( $g = -0.44$  for GaAs), and  $\sigma = 1$  ( $-1$ ) for spin-up (down) electrons. Here, we consider the antidot states coming from the lowest Landau level only. The spatial separation  $\Delta r_m \equiv r_{m+1} - r_m$  between two adjacent states depends on  $B$ . For large  $m \gg 1$ , one can show that

$$\Delta r_m \simeq \frac{\phi_0}{2\pi r_m B}. \quad (4)$$

In the case where the antidot potential  $V_{\text{AD}}(r)$  is linear over a width much greater than the separation of the states around the radius  $r_m$ , for  $m \gg 1$  (see Fig. 2), the single-particle energy gap  $\delta\epsilon_m$  between two neighboring states is proportional to  $1/B$ ,

$$\delta\epsilon_m \equiv \epsilon_{(m-1)\sigma} - \epsilon_{m\sigma} \simeq -\Delta r_m \left. \frac{dV_{\text{AD}}(r)}{dr} \right|_{r=r_m} = \frac{\phi_0}{2\pi r_m B} \left| \left. \frac{dV_{\text{AD}}(r)}{dr} \right|_{r=r_m} \right|. \quad (5)$$

The single-particle antidot states can be experimentally controlled by tuning either the antidot gate voltage or the magnetic field  $B$ . The dependence of their energies on the antidot gate voltage or on  $B$  is governed by the *quantization of enclosed magnetic flux*. For example, as  $B$  increases, the antidot states move towards the center of the antidot, keeping the average magnetic flux enclosed constant. As a consequence, the states rise up in energy, and the highest occupied states become empty one by one as they pass through the Fermi level  $E_F$ . This depopulation process is periodic in  $B$  with period  $\Delta B$ ,

$$\Delta B \simeq \frac{\phi_0}{S}, \quad (6)$$

where  $S = \pi r^2$  is the effective antidot area enclosed by the state at the Fermi level; the finite width of the spatial distribution of single-particle antidot states can slightly modify this depopulation condition because of the spatial variation of the antidot potential within the finite width. The same processes happen when the antidot gate voltage varies, changing the potential at each radius relative to  $E_F$ . We emphasize that the  $B$ -dependent depopulation of the antidot states is reminiscent of a gate-voltage controlling the states of quantum dots [5,6]. Note that when electron-electron interactions play a role, magnetic flux quantization provides still a crucial restriction on antidot states. We will return to this issue in Sec. 4.2 where excess charges around an antidot will be discussed.

The depopulation of single-particle states near the Fermi level can result in Aharonov-Bohm resonance oscillations in antidot conductance when one allows electron tunneling between the antidot states and the current-carrying extended edge channels of the 2DEG by adjusting the side gate voltages shown in Fig. 1. The conductance oscillations are the subject of the next section (2.2).

## 2.2 Aharonov-Bohm oscillations

The localized antidot states discussed in the previous section can be observed in conductance measurements when they couple to the current-carrying extended edge channels of the 2DEG. In Fig. 3, we depict schematically an experimental two-terminal setup for the measurement of electron current through an antidot in the quantum Hall regime. By tuning the side gates, one can modify the effective widths of the constrictions between the antidot and the extended edges of the 2DEG. As the widths decrease, the electron density in the constrictions becomes smaller, decreasing the constriction filling factor  $\nu_c$  from the filling factor  $\nu_{\text{bulk}} = 2\pi l_B^2 n_{\text{bulk}}$  of the bulk 2DEG, where  $n_{\text{bulk}}$  is the electron density in the bulk region. At the same time, the overlap between the antidot state at the Fermi level and the extended edge channels becomes larger, so that resonant electron tunneling becomes allowed between them. In this way, the antidot states have been experimentally studied by measuring the two-terminal conductance. In this section, we first introduce the expression [7,18,37,42,43] for the two-terminal conductance for a noninteracting antidot in the limit of zero temperature and zero bias, and discuss Aharonov-Bohm resonance oscillations in the conductance as well as the backward and forward scatterings of the extended edge channels by the antidot. Finally, we derive an expression for the two-terminal conductance in terms of the antidot Green's function, which is applicable to the cases [49] where electron interactions are important.

We consider a typical two-terminal setup shown in Fig. 3. For simplicity, the local antidot filling factor is chosen as  $\nu_c = 2$ , while the bulk filling factor of the 2DEG is  $\nu_{\text{bulk}} = 4$ . The following discussion can be easily generalized to the cases of other integer  $\nu_c$  and  $\nu_{\text{bulk}}$ . In the case of  $\nu_c = 2$  and  $\nu_{\text{bulk}} = 4$ , there are two types of extended edge channels, one from the lowest Landau level (see the channels  $a$  and  $a'$  in Fig. 3) and the other from the second lowest Landau level (the channels  $b$  and  $b'$ ). The channels  $a$  and  $a'$  pass through the antidot constriction, while  $b$  and  $b'$  are perfectly reflected at the constriction. These two different types of edge channels make electron transport through the antidot a mixture of forward and backward

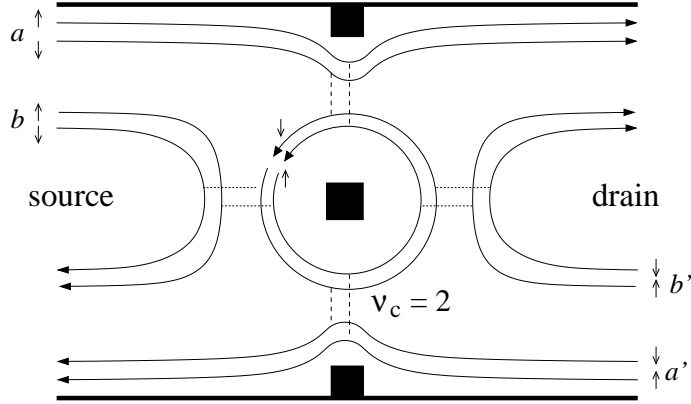


Fig. 3. A schematic diagram of a two-terminal Hall bar with an antidot. The black square at the center of the Hall bar is the antidot gate, while those attached to the upper and lower edges (thick lines) of the Hall bar represent the side gates, which control the effective widths of the constrictions between the antidot and the edges. In this diagram, the filling factor in each constriction  $\nu_c = 2$ , so the antidot states (circles) and the extended edge channels (channels  $a\sigma$  and  $a'\sigma$  with spin  $\sigma$ ) in the constrictions come from the spin-up and down lowest Landau levels. The bulk filling factor is chosen to be  $\nu_{\text{bulk}} = 4$ , so that there are two additional extended edge channels (channels  $b\sigma$  and  $b'\sigma$ ), which come from the second lowest Landau level and are perfectly reflected at the constrictions. The left side of the Hall bar is chosen to be the current source while the right is the drain. The couplings of antidot states to the channels  $a$  and  $a'$  are represented by dashed lines (intra-Landau-level coupling), and those to the channels  $b$  and  $b'$  by dotted lines (inter-Landau-level coupling). A magnetic field  $B$  is applied perpendicular to the 2DEG plane. This diagram may equivalently describe the cases of  $\nu_{\text{bulk}} > 4$  because the inter-Landau-level coupling between the antidot states and the extended edge channels coming from Landau levels higher than the second is negligible when  $B$  is strong enough.

scattering.

We first discuss a simple case where the antidot states couple only to the channels  $a$  and  $a'$  and are completely decoupled from  $b$  and  $b'$ . In this case, electrons in the channel  $a\sigma$  can be scattered into  $a'\sigma$  via a resonant antidot state with spin  $\sigma$ , thus resonant *back-scattering* occurs as shown in the following expression [7,42,43] for the total probability  $T_\sigma(E)$  of electron transmission from the source to the drain,

$$T_\sigma(E) = 1 - \frac{p_{a\sigma}p_{a'\sigma}}{1 - 2\sqrt{q_{a\sigma}q_{a'\sigma}} \cos(\Phi_{\text{AD}\sigma}(E)) + q_{a\sigma}q_{a'\sigma}}. \quad (7)$$

Here,  $E$  is the energy of incident channel,  $p_{i\sigma}$  is the scattering probability of spin- $\sigma$

electron between the channel  $i \in \{a, a'\}$  and the antidot state,  $q_{i\sigma} = 1 - p_{i\sigma}$ , and  $\Phi_{\text{AD}\sigma}(E)$  is the phase accumulated along the complete orbit of the antidot state, which includes the phase shifts acquired in the scattering processes between the channels and the antidot. Note that the energy dependence of  $p_{i\sigma}$  is ignored. A localized antidot state comes on to resonance when the phase accumulation is an integer multiple of  $2\pi$ , *i.e.*  $\Phi_{\text{AD}\sigma} = 2\pi l$ , causing a minimum in  $T_\sigma$ . We note that the transmission (7) has the inverse Breit-Wigner resonance line shape around the resonance energy  $E_{\text{res}}$  in the limit of  $\Gamma$  smaller than the single-particle level spacing since

$$T_\sigma(E) \simeq 1 - \frac{\Gamma_\sigma^a \Gamma_\sigma^{a'}}{(E - E_{\text{res}})^2 + (\Gamma_\sigma^a + \Gamma_\sigma^{a'})^2/4}. \quad (8)$$

Here,  $\Gamma_\sigma^i = p_{i\sigma}(dE/d\Phi_{\text{AD}\sigma})$  is the broadening width of the resonance due to the coupling to the channel  $i \in \{a, a'\}$ , and we have used the approximation that  $1 - \cos(\Phi_{\text{AD}\sigma}(E)) \simeq (d\Phi_{\text{AD}\sigma}/dE)^2(E - E_{\text{res}})^2/2$  around  $E = E_{\text{res}}$ .

There is also a simple case of resonant *forward* scattering, where the antidot states couple only to the channels  $b$  and  $b'$  and are completely decoupled from  $a$  and  $a'$ . In this case, the total transmission probability  $T_\sigma$  from the source to the drain can be obtained as

$$T_\sigma(E) = 1 + \frac{p_{b\sigma} p_{b'\sigma}}{1 - 2\sqrt{q_{b\sigma} q_{b'\sigma}} \cos(\Phi_{\text{AD}\sigma}(E)) + q_{b\sigma} q_{b'\sigma}}. \quad (9)$$

Here,  $p_{i\sigma}$  is the scattering probability of spin- $\sigma$  electrons between channel  $i \in \{b, b'\}$  and the antidot state, and  $q_{i\sigma} = 1 - p_{i\sigma}$ . The first term of Eq. (9) comes from the perfect transmission of the channels  $a$  and  $a'$ . The resonances occur with the maximum value of  $T_\sigma$  at the same condition of  $\Phi_{\text{AD}\sigma} = 2\pi l$  as the above back-scattering case.

In the general case where the antidot couples to both types of channel ( $a, a'$ ) and ( $b, b'$ ), the total transmission from the source to the drain is a combination of the forward and backward scattering given by [43]

$$T_\sigma(E) = 1 + \frac{q_{a\sigma} + q_{a'\sigma} + q_{a\sigma} q_{a'\sigma} (q_{b\sigma} q_{b'\sigma} - q_{b\sigma} - q_{b'\sigma}) - 1}{1 - 2\sqrt{q_{a\sigma} q_{a'\sigma} q_{b\sigma} q_{b'\sigma}} \cos(\Phi_{\text{AD}\sigma}(E)) + q_{a\sigma} q_{a'\sigma} q_{b\sigma} q_{b'\sigma}}. \quad (10)$$

On resonance,  $T_\sigma$  can be either larger or smaller than 1, determined by the competition between the antidot coupling strengths  $\Gamma_\sigma^i$  to the extended edge channels  $i \in \{a, a', b, b'\}$ . The phase accumulation  $\Phi_{\text{AD}\sigma}$  depends on the magnetic field  $B$  as

$\Phi_{\text{AD}\sigma} = 2\pi BS/\phi_0 + \Phi_{\text{AD}\sigma,0}$ , where  $\Phi_{\text{AD}\sigma,0}$  is a phase independent of  $B$ . Thus as a function of  $B$  the transmission shows Aharonov-Bohm oscillations with period  $\Delta B$  given by Eq. (6) and line shape given by Eq. (10). This noninteracting description of the Aharonov-Bohm oscillations will be used to analyze experimental data in Sec. 3. However, this noninteracting model fails to explain all the data, so we need an expression for the transmission that can be used for interacting electrons; this will be derived based on a Green's-function method in the remaining parts of this section.

Below, for the antidot system shown in Fig. 3, we will derive the total transmission from the source to the drain in terms of the Green's function of the antidot in the limit of zero temperature and zero bias. Following Ref. [62], we start with the S-matrix of the extended edge channels  $i \in \{a, a', b, b'\}$ . Because there is no spin-flip process at each single-electron tunneling event (in the absence, for example, of spin-orbit coupling), the S-matrix does not connect channels of different spin, and it has the following form,

$$\begin{aligned}\vec{A}_{\text{out},\sigma} &= \tilde{S}_\sigma \vec{A}_{\text{in},\sigma}, \\ \vec{A}_{\text{in},\sigma}^\top &= (u_{a\sigma}, u_{b\sigma}, u_{a'\sigma}, u_{b'\sigma}), \\ \vec{A}_{\text{out},\sigma}^\top &= (v_{a\sigma}, v_{b\sigma}, v_{a'\sigma}, v_{b'\sigma}),\end{aligned}$$

where  $\vec{A}_{\text{in},\sigma}$  is the incoming spin- $\sigma$  state vector to the antidot,  $\vec{A}_{\text{out},\sigma}$  is the outgoing state vector, and  $\vec{A}_{\text{in}/\text{out},\sigma}^\top$  is the transpose of  $\vec{A}_{\text{in}/\text{out},\sigma}$ . The detailed form of the S-matrix can be found as

$$\tilde{S}_\sigma = \tilde{I} - 2\pi i N_\sigma \mathcal{G}_\sigma(E + i\delta) \begin{pmatrix} t_{a\sigma}^2 & t_{b\sigma} t_{a\sigma} & t_{a'\sigma} t_{a\sigma} & t_{b'\sigma} t_{a\sigma} \\ t_{a\sigma} t_{b\sigma} & t_{b\sigma}^2 & t_{a'\sigma} t_{b\sigma} & t_{b'\sigma} t_{b\sigma} \\ t_{a\sigma} t_{a'\sigma} & t_{b\sigma} t_{a'\sigma} & t_{a'\sigma}^2 & t_{b'\sigma} t_{a'\sigma} \\ t_{a\sigma} t_{b'\sigma} & t_{b\sigma} t_{b'\sigma} & t_{a'\sigma} t_{b'\sigma} & t_{b'\sigma}^2 \end{pmatrix}, \quad (11)$$

where  $\tilde{I}$  is the identity matrix,  $N_\sigma(E)$  is the density of states of noninteracting spin- $\sigma$  electrons of each extended edge channel (the channel-dependence of  $N_\sigma(E)$  is ignored), and  $\mathcal{G}_\sigma(E + i\delta)$  is the full Green's function of the antidot. Also,  $t_{i\sigma}$  is the hopping energy between an antidot state with spin  $\sigma$  and the edge channels  $i\sigma$ ,  $i \in \{a, a', b, b'\}$ . From  $\tilde{S}_\sigma$ , one can define the transmission matrix  $\tilde{T}_\sigma$ :

$$\begin{aligned}
(v_{a\sigma}, v_{b'\sigma})^T &= \tilde{T}_\sigma (u_{a\sigma}, u_{b\sigma})^T, \\
\tilde{T}_\sigma &= \begin{pmatrix} 1 - 2\pi i t_{a\sigma}^2 N_\sigma \mathcal{G}_\sigma & -2\pi i t_{a\sigma} t_{b\sigma} N_\sigma \mathcal{G}_\sigma \\ -2\pi i t_{b'\sigma} t_{a\sigma} N_\sigma \mathcal{G}_\sigma & -2\pi i t_{b'\sigma} t_{b\sigma} N_\sigma \mathcal{G}_\sigma \end{pmatrix}.
\end{aligned} \tag{12}$$

The total transmission  $T_\sigma$  of the channels  $a\sigma$  and  $b\sigma$  incoming from the source to the channels  $a\sigma$  and  $b'\sigma$  outgoing to the drain can be found as  $T_\sigma = \text{Tr}(\tilde{T}_\sigma^\dagger \tilde{T}_\sigma)$ .

To derive  $T_\sigma$  further, we use the imaginary part of the self-energy of  $\mathcal{G}_\sigma(E_F)$ ,

$$\Im \Sigma_\sigma(E_F) = -\pi(t_{a\sigma}^2 + t_{b\sigma}^2 + t_{a'\sigma}^2 + t_{b'\sigma}^2)N_\sigma(E_F), \tag{13}$$

and the occupation number  $\langle n_\sigma \rangle$  of the antidot,

$$\langle n_\sigma \rangle = \pi^{-1} \Im(\ln \mathcal{G}_\sigma(E_F + i\delta)). \tag{14}$$

After some trivial algebra, one can find  $T_\sigma$  in terms of  $\theta_\sigma = \pi \langle n_\sigma \rangle$  as

$$\begin{aligned}
T_\sigma &= 1 + \frac{4(t_{b\sigma}^2 t_{b'\sigma}^2 - t_{a\sigma}^2 t_{a'\sigma}^2) \sin^2 \theta_\sigma}{(t_{a\sigma}^2 + t_{b\sigma}^2 + t_{a'\sigma}^2 + t_{b'\sigma}^2)^2} \\
&= 1 + \frac{4(\Gamma_\sigma^b \Gamma_\sigma^{b'} - \Gamma_\sigma^a \Gamma_\sigma^{a'}) \sin^2 \theta_\sigma}{(\Gamma_\sigma^a + \Gamma_\sigma^b + \Gamma_\sigma^{a'} + \Gamma_\sigma^{b'})^2}.
\end{aligned} \tag{15}$$

Then, in the linear-response regime at zero temperature, the two-terminal conductance  $G_{\text{ad}}$  of the antidot system shown in Fig. 3 is immediately written as

$$G_{\text{ad}} = \sum_\sigma G_\sigma = \sum_\sigma \frac{e^2}{h} T_\sigma. \tag{16}$$

Here, we provide a simple application of the transmission (15). In the weak coupling regime, the antidot Green's function and  $\sin^2 \theta_\sigma$  can be written around a resonance energy  $E_{\text{res}}$  as

$$\mathcal{G}(E) = \frac{1}{E - E_{res} - i\Im\Sigma_\sigma},$$

$$\sin^2 \theta_\sigma = \frac{(\Im\Sigma_\sigma)^2}{(E - E_{res})^2 + (\Im\Sigma_\sigma)^2}. \quad (17)$$

If one assumes that the antidot is decoupled from the edge channels  $b$  and  $b'$ , *i.e.*,  $\Gamma_\sigma^b = \Gamma_\sigma^{b'} = 0$ , the expressions (15) and (17) lead to the inverse Breit-Wigner line shape equivalent to Eq. (8), which describes the backscattering. On the other hand, if one assumes  $\Gamma_\sigma^a = \Gamma_\sigma^{a'} = 0$ , one can find the expression for the forward scattering as well.

The expression (15) for the total transmission is applicable for interacting electrons. However, in order to use it, one has to know the antidot Green's function or  $\theta_\sigma$ . For example,  $\theta_\sigma$  has been calculated [49] by using the numerical renormalization group method (see Sec. 4.4), and the resulting line shape has been found to reproduce the experimental Kondo features [25].

### 3 Experimental signatures of electron interactions in antidots

In the previous section, the single-particle antidot energy levels and the Aharonov-Bohm forward and backward scattering by an antidot have been discussed within a noninteracting model. In experiments, Aharonov-Bohm oscillations with an antidot were first observed by Smith and his coworkers [9]. Since then, the Aharonov-Bohm effect has been intensively investigated experimentally [1,2,17,18,19,20,21,22,23,24,25,26] in the integer quantum Hall regime and revealed some interesting features in the period, the line shape, and the temperature or bias dependence of the Aharonov-Bohm conductance oscillations that cannot be explained within the noninteracting model.

In this section, we describe the experimental work devoted to electron interactions in an antidot in the integer quantum Hall regime and compare the observations with the noninteracting model. We discuss typical experimental setups (Sec. 3.1), simple Aharonov-Bohm oscillations, including the detection of the oscillation of the Fermi energy [19] (Sec. 3.2), direct evidence of the antidot charging effect [22] found using a noninvasive voltage probe (Sec. 3.3), the  $h/2e$  Aharonov-Bohm oscillations in  $\nu_c = 2$  antidots [1,2,23,26] (Sec. 3.4), the spectator behavior of the molecular modes in antidot molecules [28] (Sec. 3.5), the signature of electron interactions found in the line shape [21] (Sec. 3.6), an experimental search for the compressible regions

around an antidot [23,24,58,59,61] (Sec. 3.7), and the antidot Kondo effect [25] (Sec. 3.8).

### 3.1 Typical experimental setup

The typical experimental setup of an antidot is as follows. The antidot potential and the constrictions (see Fig. 3) can be formed by using Schottky gates and/or shallow etching on the surface of a high-mobility GaAs-Al<sub>x</sub>Ga<sub>1-x</sub>As heterostructure. The size or the energy levels of the antidot and the electrical widths of the constrictions can be tuned by applying negative voltages to the gates. The typical carrier concentration and mobility are  $(1 - 4) \times 10^{15} \text{ m}^{-2}$  and  $> 100 \text{ m}^2/\text{Vs}$ , respectively. The typical lithographic width of the antidot gate (or etched pit) is  $0.2 - 0.3 \mu\text{m}$ , and the lithographic width of the side constrictions is  $0.4 - 0.8 \mu\text{m}$ . A negative gate voltage of the order of  $-1 \text{ V}$  creates an antidot potential of effective radius  $r_{\text{AD}} \sim 0.3 - 0.4 \mu\text{m}$  at the Fermi level. We note that the Aharonov-Bohm period in magnetic field for adding one more flux quantum  $\phi_0$  to a loop of radius  $r_{\text{AD}} \sim 0.3 \mu\text{m}$  is  $\sim 15 \text{ mT}$ . The conductance of the antidot geometry has been measured at temperatures lower than  $100 \text{ mK}$  using standard low-bias ac lock-in techniques. The constriction filling factors are usually adjusted to  $\nu_c = 1$  or  $2$ , while the bulk filling factor  $\nu_{\text{bulk}}$  is larger than  $\nu_c$ .

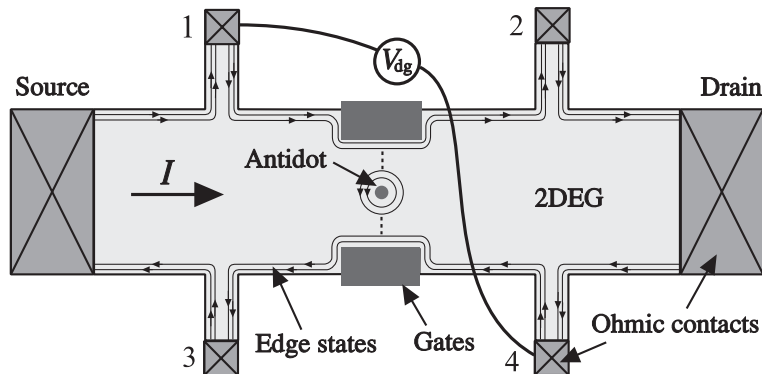


Fig. 4. A typical experimental setup for antidot conductance measurements.

The antidot conductance can be measured in various ways, two-terminally or four-terminally. Following the Landauer-Büttiker formula [63], the two-terminal antidot conductance in the absence of resonances with small source-drain bias  $V$  and measured current  $I$  gives



$$G_{\text{ad-2T}} = \frac{I}{V} = \nu_c \frac{e^2}{h}. \quad (18)$$

The two-terminal conductance is useful, and intuitive, because this background conductance is quantized and reveals the filling factor in whichever antidot constriction is wider. Resonances through the antidot states appear as peaks or dips on the background conductance, depending on the nature of the scattering, following Eq. (16). However, actual two-terminal measurements include series resistance, which prevents the exact quantization of the background conductance. On the other hand, four-terminal measurements of longitudinal conductance (the derivation of which is provided in the next paragraph)

$$G_{\text{ad-4T}} = \frac{I}{V_L} = \left( \frac{1}{\nu_c} - \frac{1}{\nu_{\text{bulk}}} \right)^{-1} \frac{e^2}{h}, \quad (19)$$

where  $V_L$  is the longitudinal voltage drop, do not suffer the effect of series resistance. However, the background conductance is not quantized and the bulk filling factor needs to be taken into account in extracting the information on the antidot filling factor. The effect of the bulk filling factor can be removed by adding in the Hall voltage with the correct sign, by measuring the diagonal voltage drop  $V_{\text{dg}}$ , as shown in Fig. 4:

$$G_{\text{ad-dg}} = \frac{I}{V_{\text{dg}}} = \nu_c \frac{e^2}{h}. \quad (20)$$

This is effectively equal to the ideal two-terminal conductance (without the effect of series resistance). This feature comes from the chiral and adiabatic transport of edge channels, which does not produce any voltage drop between the voltage-probe reservoir 1 (4) and the source (drain).

Before closing this subsection, we derive  $G_{\text{ad-4T}}$ , based on the Landauer-Büttiker formalism [63]. In the formalism, the current at a reservoir  $l$  is written as

$$I_l = \frac{e}{h} \sum_{l_1 \neq l} (T_{l \rightarrow l_1} \mu_l - T_{l_1 \rightarrow l} \mu_{l_1}),$$

where  $T_{l \rightarrow l_1}$  is the total transmission from reservoir  $l$  to  $l_1$  and  $\mu_{l(l_1)}$  is the electrochemical potential of reservoir  $l$  ( $l_1$ ). The first term in the above relation shows the

current outgoing from the reservoir  $l$  to  $l_1$  while the second means the contribution incoming from  $l_1$  to  $l$ . This relation can be applied for the antidot setup in Fig. 4, taking into account the chiral and adiabatic nature of edge-channel transport, as

$$\begin{aligned}
I_{\text{source}} = I &= \frac{e}{h}(\nu_{\text{bulk}}\mu_{\text{source}} - \nu_{\text{bulk}}\mu_3), \\
I_1 = 0 &= \frac{e}{h}(\nu_{\text{bulk}}\mu_1 - \nu_{\text{bulk}}\mu_{\text{source}}), \\
I_2 = 0 &= \frac{e}{h}[\nu_{\text{bulk}}\mu_2 - \nu_c\mu_1 - (\nu_{\text{bulk}} - \nu_c)\mu_4], \\
I_3 = 0 &= \frac{e}{h}[\nu_{\text{bulk}}\mu_3 - \nu_c\mu_4 - (\nu_{\text{bulk}} - \nu_c)\mu_1], \\
I_4 = 0 &= \frac{e}{h}(\nu_{\text{bulk}}\mu_4 - \nu_{\text{bulk}}\mu_{\text{drain}}), \\
I_{\text{drain}} = -I &= \frac{e}{h}(\nu_{\text{bulk}}\mu_{\text{drain}} - \nu_{\text{bulk}}\mu_2),
\end{aligned}$$

where  $\mu_{\text{source}}$ ,  $\mu_{\text{drain}}$ , and  $\mu_l$  are the electrochemical potentials of the source, drain and reservoir  $l = 1, 2, 3, 4$ , respectively. Here,  $I_{l=1,2,3,4} = 0$  since the reservoirs  $l$  are voltage probes. From the above set of current relations, one can arrive at  $\mu_2 - \mu_1 = (\nu_{\text{bulk}}^{-1} - \nu_c^{-1})(h/e)I$ , from which  $G_{\text{ad-4T}} = (\nu_c^{-1} - \nu_{\text{bulk}}^{-1})^{-1}(e^2/h)$ .  $G_{\text{ad-2T}}$  and  $G_{\text{ad-dg}}$  can be derived in a similar manner.

### 3.2 Simple Aharonov-Bohm oscillations

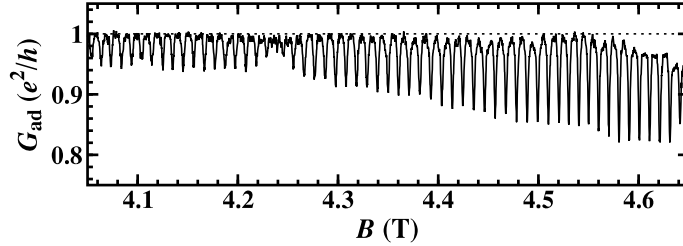


Fig. 5. Typical Aharonov-Bohm oscillations of conductance  $G_{\text{ad}}$  in an antidot with  $\nu_c = 1$ . Conductance dips appear from the  $\nu_c = 1$  plateau (dotted line), indicating that back-scattering is dominant. From [64].

Figure 5 shows typical resonance structure in the conductance  $G_{\text{ad}}$  for an antidot with  $\nu_c = 1$ , as a function of magnetic field. Back-scattering causes periodic Aharonov-

Bohm resonance dips from the  $\nu_c = 1$  plateau. From the periodicity of 10.5 mT, the effective antidot radius is estimated to be  $0.35 \mu\text{m}$  [see Eq. (6)].

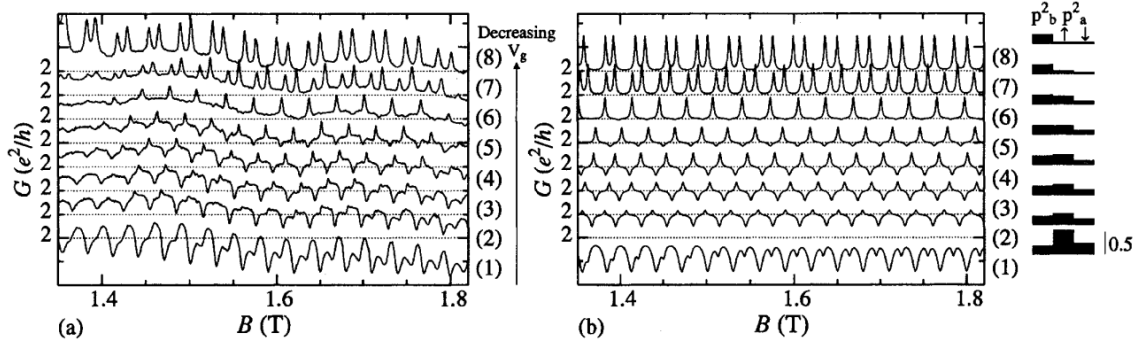


Fig. 6. (a) Aharonov-Bohm oscillations of antidot conductance  $G$  with  $\nu_c = 2$ , which show the transition from conductance peaks to dips as the antidot gate voltage is increased negatively down the curves. The curves are offset vertically for clarity. (b) Corresponding model conductance curves and scattering probabilities. From [18].

The antidot states and their coupling to the extended edge channels can be studied from the periodic nature of the Aharonov-Bohm oscillations, the line shapes of the peaks or the dips, and their heights. For example, one can study the coupling of the antidot states to the extended edge channels by varying the antidot gate voltage. As the magnitude of the gate voltage decreases, the size of the antidot is reduced and the coupling between the antidot states and the extended edge channel  $a$  passing through the constrictions (see Fig. 3) becomes weaker. As we have seen in Sec. 2, the result is that the forward scattering is favored more as the gate voltage becomes less negative. Such competition [see Eq. (10)] between forward and backward scattering was first studied experimentally in a systematic way by Mace and coworkers [18].

In Fig. 6, the antidot gate voltage is made more negative for the lower traces. In the topmost curve, paired peaks appear from the  $\nu_c = 2$  plateau. These peaks are caused by resonant transmission through the two spin states of the lowest Landau level (we call these edge states 1 and 2, see Fig. 7); the left-hand peak of the pairs is via spin-down states (higher Zeeman energy, edge state 2), and the right-hand peak is via spin-up states (lower Zeeman energy, edge state 1). Let us call the spin-up and spin-down edge states of the next Landau level 3 and 4, respectively. We denote inter-edge-state scattering from edge state 4 to 2 as 4–2 and similarly for 3–1. These processes scatter between Landau levels, preserving the spin. The two peaks have similar amplitudes because the tunneling distances of 4–2 and 3–1 scattering are almost the same (see Fig. 7). As the antidot voltage is increased negatively,

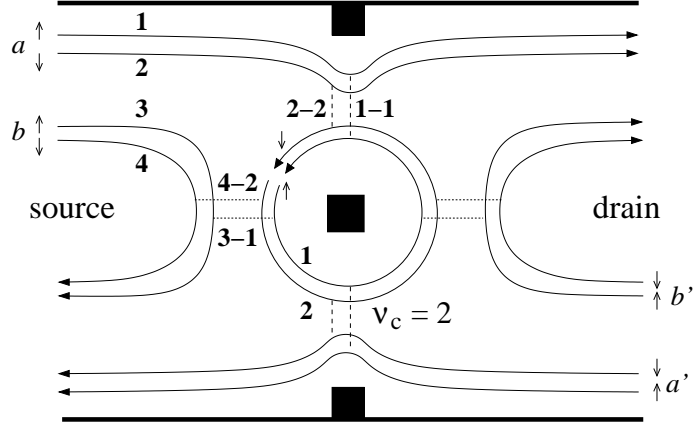


Fig. 7. The same schematic diagram of an antidot with  $\nu_c = 2$  as in Fig. 3, except for introducing the following notation for the Landau levels. The states coming from the spin-up and spin-down states of the lowest Landau level are denoted as 1 and 2, respectively, and those from the spin-up and spin-down states of the next Landau level as 3 and 4, respectively. This notation is convenient to describe the scattering between the antidot states and the extended edge channels. The inter-Landau-level coupling between the antidot spin-up (down) state and the channel  $b \uparrow$  ( $b \downarrow$ ) is represented as 3-1 (4-2) scattering. Similarly, the intra-Landau-level coupling between the antidot spin-up (down) state and the channel  $a \uparrow$  ( $a \downarrow$ ) is represented as 1-1 (2-2) scattering.

increasing the antidot size, these resonances shift towards smaller magnetic field, as each state moves up in energy to keep the enclosed flux constant. As the antidot voltage is increased further, the amplitude of each left-hand peak starts to decrease, and eventually the peaks turn into dips. The right-hand peak follows the same trend at more negative antidot gate voltages. This behavior can be fully understood by the noninteracting model. As the size of the antidot increases, the constriction width becomes narrower, so the spin-down state starts to couple with the corresponding extended edge channel transmitted through the constrictions, of the same Landau level and spin. We denote this tunneling as 2-2, and similarly 1-1 for the other spin. This back-scattering is through exactly the same resonant state that gives a left-hand resonant transmission (4-2) peak. In the absence of 4-2 tunneling, this would give rise to a dip. With both 4-2 and 2-2 present, the dip and peak have the same linewidth, as that is determined by the state's lifetime. The dip and peak compete, reducing the peak height, and eventually the peak turns into a dip as 2-2 becomes dominant. The back-scattering of the spin-up state (1-1) starts at a later stage, when the constrictions are narrower, since the tunneling distance for 1-1 is longer than for 2-2 (see Fig. 7).

We note that Aharonov-Bohm oscillations of antidot conductance can be used to detect the oscillation of the Fermi energy in the 2D system surrounding it [19]. The deviation of the period of the Aharonov-Bohm oscillations from the average periodicity was found to oscillate in synchrony with the bulk Shubnikov–de-Haas oscillations (see Fig. 8). Numerical calculations were used to show that the result was consistent with the oscillation of the Fermi energy and the concomitant oscillation of the density of states there.

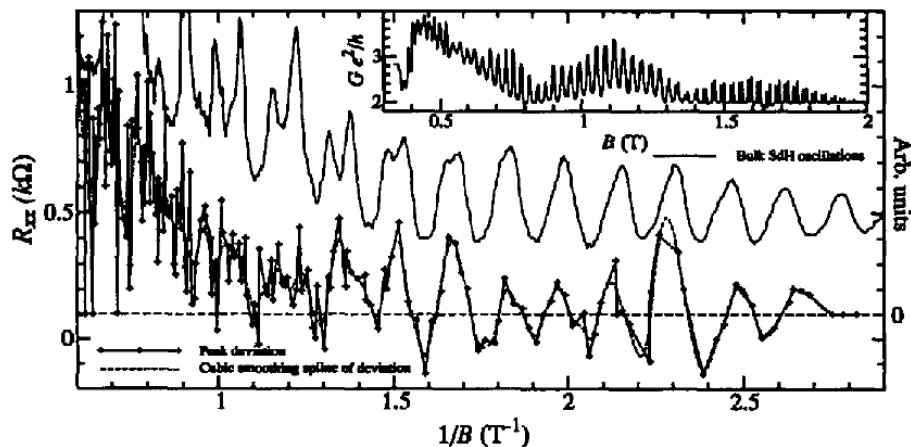


Fig. 8. Inset: A typical conductance trace in which an aperiodicity in the Aharonov-Bohm oscillations is clearly seen near 0.6 T. Upper solid line: resistance  $R_{xx}$  of the 2D region with that antidot gate voltage set to zero. (At high field, the antidot is defined at zero gate voltage, accounting for the absence of zeros.) Lower solid line with points (right-hand axis): deviation of the peak position against peak index, derived by removing a smoothed background; four different antidot radii were used to obtain more points. Dashed line: cubic smoothing spline performed on the solid line with points. From [19].

As in these low-field examples, much can be learned about the behavior and properties of antidot states in each field range by studying the variation of the resonances as they are tuned with gate voltages. Some experimental observations [17,18] can be understood within the noninteracting electron model in Sec. 2, while others require an explanation taking electron interactions into account. In the following sections, we describe the experimental data that cannot be explained by a simple noninteracting model, starting with the observation of the antidot charging effect.

### 3.3 Detection of antidot charging

The charging effect is a ubiquitous feature of quantum dots, almost isolated small-size potential wells weakly coupled to reservoirs. The large capacitive energy required to add an electronic charge to the dot, and electron-electron interactions inside the quantum dots, can prevent electron tunneling between the dot and the reservoirs, resulting in Coulomb-blockade phenomena [5,6].

An antidot is an open system and does not electrostatically confine any electrons. However, a sufficiently strong perpendicular magnetic field applied to the antidot system can confine electrons around the antidot and result in the formation of localized antidot states as discussed in Sec. 2. Therefore, one may expect that the Coulomb interactions between the localized antidot states cannot be ignored and could play some role. Indeed, experimental findings of  $h/2e$  Aharonov-Bohm oscillations [1,2] with a single antidot and unexpected behavior of molecular states in two coupled antidots (antidot molecule) [28] enhanced this expectation, which will be reviewed in the next two sections (Secs. 3.4 and 3.5). Here, we will focus on the observation of the direct evidence of the charging effect in the antidot.

Direct evidence of the antidot charging effect was found in Ref. [22] using a noninvasive voltage probe [65]. The noninvasive voltage detection was made (see Fig. 9) by fabricating a detector constriction next to an antidot system, the lithographic dimensions of which are similar to those described in Sec. 3.1. The detector constriction is separated from the antidot system by the separation gate  $G_{\text{sep}}$  of width  $0.1\mu\text{m}$ , and the resistance  $R_{\text{det}}$  of the constriction is adjusted to be very sensitive to the variations of charges nearby by tuning the detector gate to nearly pinch off that channel. The variation of the total antidot charge is visible in the measurement of  $R_{\text{det}}$ . Note that a similar noninvasive voltage probe was first used by Field and his coworkers to detect charge oscillations in a quantum dot [65].

Here, in order to enhance the detector sensitivity, the detector transresistance  $-dR_{\text{det}}/dV_{G-\text{side}}$  was measured by modulating the voltage on  $G_{\text{side}}$  at a low frequency as shown in Figs. 9(a) and (b) measured at two different antidot filling factors. Dips in  $-dR_{\text{det}}/dV_{G-\text{side}}$  appear in phase with the oscillations in the antidot transconductance  $dG_{\text{ad}}/dV_{G-\text{side}}$ , which was measured simultaneously. The relations between the transresistance/transconductance line shapes and the resistance/conductance line shapes are shown in Fig. 9(c). These show that the observed dips in the detector transresistance correspond to sawtooth oscillations in the detector resistance, which

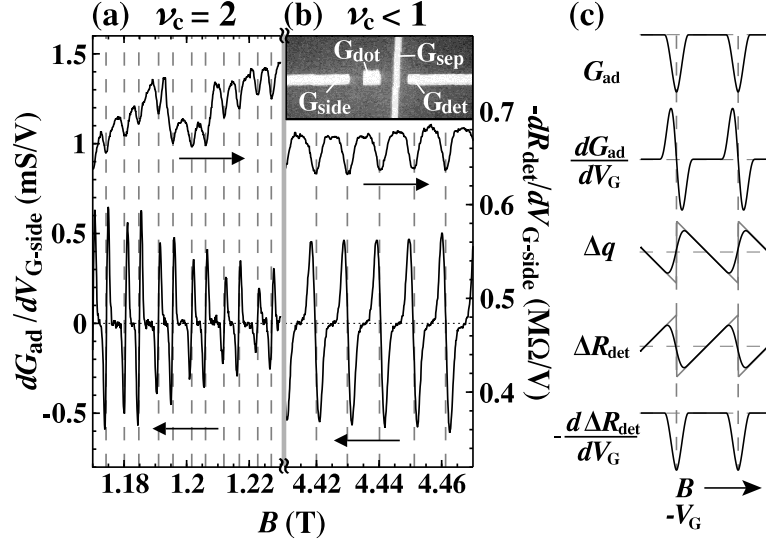


Fig. 9. An antidot setup with a noninvasive voltage detector and the simultaneous measurement of the conductance  $G_{\text{ad}}$  of the antidot system and the detector resistance  $R_{\text{det}}$ , as a function of magnetic field  $B$ . Left panel:  $dG_{\text{ad}}/dV_{G\text{-side}}$  and  $-dR_{\text{det}}/dV_{G\text{-side}}$  are shown in the two different regimes of antidot filling factors (a)  $\nu_c = 2$  and  $\nu_{\text{bulk}} = 7$  and (b)  $\nu_c < 1$  and  $\nu_{\text{bulk}} = 2$ . Here,  $V_{G\text{-side}}$  is the side gate voltage. Vertical dashed lines show that the dips of  $-dR_{\text{det}}/dV_{G\text{-side}}$  coincide with the zeros of  $dG_{\text{ad}}/dV_{G\text{-side}}$ , showing that the Aharonov-Bohm oscillation of  $G_{\text{ad}}$  is accompanied by the relaxation and accumulation of the excess charges  $\Delta q$  around the antidot. Inset: Scanning electron micrograph of the device. Right panel (c): Illustration of the relation between the line shapes of  $G_{\text{ad}}$ ,  $dG_{\text{ad}}/dV_{G\text{-side}}$ ,  $\Delta q$ ,  $R_{\text{det}}$ , and  $d\Delta R_{\text{det}}/dV_G$ . From Ref. [22].

are the evidence of the steady accumulation and sudden relaxation (presumably in units of  $e$ ) of some excess charge  $\Delta q$  near the detector constriction. The discrete steps in the charge oscillations coincide with the resonances in the antidot conductance, as expected for Coulomb blockade oscillations. Therefore it is concluded that the source of the excess charge is the antidot.

The above result confirms the following interpretation [1,22,49]. As  $B$  increases, all the states encircling the antidot move inwards to keep the enclosed flux  $BS_m$  constant, while the density of the positive background charges (which come from ionized donors and gate voltages and preserve the total charge neutrality of the whole system) is fixed (see Fig. 10). If the occupation of the antidot states does not vary during their movement, excess (negative) charge  $\Delta q$  accumulates around the antidot. The excess charge cannot be screened by the electrons in completely filled (incompress-

ible) states around the antidot. The antidot therefore behaves like a quantum dot, with a capacitive energy of  $\Delta q^2/(2C)$ , where  $C$  is an effective capacitance of the antidot. The accumulated excess charge cannot relax because of an energy cost for removing an electron, until  $\Delta q$  reaches  $-e/2$ , at which point the total energy of the system is the same as for an excess charge of  $\pm e/2$ , and an electron can leave, making  $\Delta q = e/2$ ; here, the effect of the single-particle energy is ignored for simplicity. The process repeats, with electrons tunneling from one lead to the other via this resonant state with no energy cost, giving rise to a peak or dip in  $G_{\text{ad}}$ . Further increase of  $B$  again gives rise to a positive energy for adding or removing an electron, and so the system goes off resonance. Resonant tunneling repeats with the periodicity of the movement of the single-particle states, as each moves up to the position formerly occupied by its neighbor. This corresponds to adding  $h/e$  of flux to the area enclosed by a state at the Fermi energy, and so we have the usual  $h/e$  Aharonov-Bohm periodicity. Rigorous discussion of the resonant scattering will appear in Sec. 4.2, where electron interactions will be taken into account.

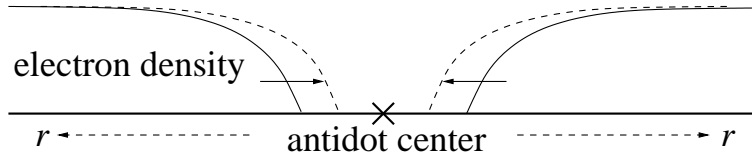


Fig. 10. Schematic diagram of the accumulation of excess charge  $\Delta q$  around the antidot as the magnetic field increases. The electron density shift results from the enclosed magnetic flux movement of the discrete single-particle states to keep the enclosed magnetic flux constant. From Ref. [49].

The antidot charging effect can be further analyzed from the experimental observation [22] of the dependence of the differential conductance  $dG_{\text{ad}}/dV_{\text{sd}}$  on the magnetic field  $B$  and the source-drain dc bias  $V_{\text{sd}}$ , which is shown in Fig. 11. The plots show “Coulomb diamonds”, which have been used to investigate Coulomb blockade in quantum dots [5,6], with the net charge being changed by the gate voltage rather than the magnetic field. From the height of the diamonds, one can extract the energy  $\Delta E_{\text{tot}} = e^2/C + \delta\epsilon$  to add one electron to the dot, where  $e^2/C$  is the charging energy of the dot and  $\delta\epsilon$  is the level spacing of the single-particle states with the same spin. One can apply the same model to an antidot to see whether there is any charging energy. In Fig. 11(a)-(c), there are spin-split resonances since the antidot has both spin states in those cases. The spin-split resonances are manifested by the two neighboring bigger and smaller diamonds, the sizes of which are expected to correspond to  $e^2/C + \delta\epsilon - E_Z$  and  $e^2/C + E_Z$ . Here,  $E_Z = \epsilon_{\downarrow}^Z - \epsilon_{\uparrow}^Z$  is the Zeeman splitting. The average size of  $\Delta E_{\text{tot}}$  for spin-up and down diamonds is  $e^2/C + \delta\epsilon/2$



and is found to be almost constant throughout the range in Fig. 11(a)-(c). Its value  $\Delta E_{\text{tot}} \simeq 140 \mu\text{eV}$  is in good agreement with the analysis of the temperature dependence of the Aharonov-Bohm scattering by the antidot. Another important result of the diamond plots is that they reveal the excitation spectrum of the antidot as shown in the additional parallel lines to the smaller diamonds. The energy gap between the parallel lines and the diamonds can be interpreted as  $\delta\epsilon - E_Z$  or  $E_Z$ , depending on around which diamonds the excitation line appears. This allows one to deduce the charging-energy contribution to  $\Delta E_{\text{tot}}$ .

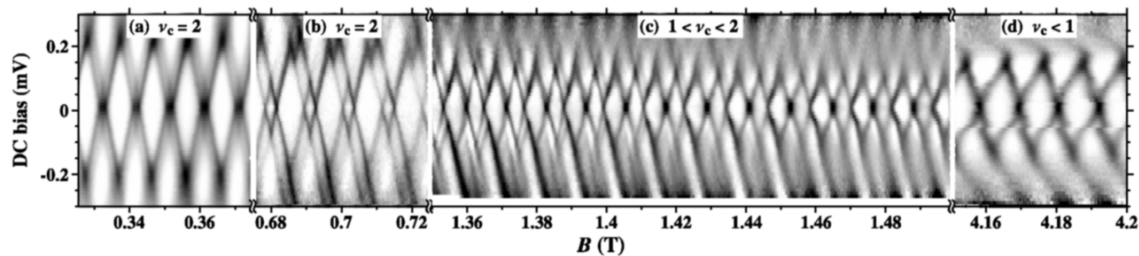


Fig. 11. Coulomb-diamond plots for the antidot. The differential conductance of the antidot is plotted as a function of the magnetic field  $B$  and the source-drain dc bias. The same gate voltages are used throughout. Dark regions correspond to positions of resonance peaks [in (a) and (b)] or dips [in (c) and (d)]. The background variation in the signal was subtracted to increase the contrast. From Ref. [22].

The roughly constant value of  $\Delta E_{\text{tot}}$  throughout a wide range of magnetic field can be understood as a coincidence, from the expectation that the magnetic field dependence of  $\delta\epsilon$  scales as  $\sim 1/B$  for the antidot with a constant potential slope [see Eq. (5)], while  $e^2/C$  can increase for larger  $B$  due to stronger magnetic confinement. The analysis in Ref. [22] indicates  $e^2/C \sim 100 - 120 \mu\text{eV}$  at  $B = 1.4 \text{ T}$ .  $\Delta E_{\text{tot}}$  drops rapidly in the regimes where the antidot couples strongly with the extended edge channels. This is because the coupling enhances the capacitance, and thus the charging energy becomes smaller in those regimes.

All these observations show that charging can indeed play an important role in the antidot, depending on the relative sizes of the single-particle and charging energies. The energy levels of the antidot can be strongly affected by the charging energy, the positions of the Aharonov-Bohm resonances may be determined by the net charge around the antidot, and there is an accompanying accumulation and relaxation of excess charge around the antidot. The importance of this finding is that antidot Aharonov-Bohm oscillations are not only governed by the quantization of enclosed magnetic flux, but also by the capacitive energy of the system. This charging model

has led to the understanding of various effects in antidots, as described in the following sections.

### 3.4 $h/2e$ Aharonov-Bohm oscillations

In a quantum dot at a high magnetic field, the Aharonov-Bohm effect can occur in combination with Coulomb charging [66,67,68,69]. When the dot has two spin species, *i.e.*, when the filling factor in the dot is two, it was found that resonances from one spin species occur exactly halfway between the neighboring resonances of the second spin species. To explain this feature, a charging model of the dot was proposed [70,71]. In this section, we will describe similar behavior [1,2,23] observed in an antidot with  $\nu_c = 2$ . In certain ranges of magnetic field and antidot gate voltage, the  $\nu_c = 2$  antidot can show resonant tunneling with period in magnetic field  $\Delta B = \phi_0/(2S) = h/(2eS)$ , which is exactly the half the Aharonov-Bohm period in Eq. (6). Such observation of the  $h/2e$  Aharonov-Bohm oscillations and the spectator behavior of the antidot molecular states, which will be reviewed in the next section, cannot be explained by the noninteracting model, and they provided a strong motivation of studying the antidot charging effect [22] reviewed in Sec. 3.3.

The top three curves in Fig. 12 show typical experimental data of the  $h/2e$  Aharonov-Bohm oscillations, which appear in the antidot with  $\nu_c = 2$ . Since there are states of each spin orientation encircling the antidot, one may conjecture that the  $h/2e$  oscillations occur as a result of two  $h/e$  oscillations out of phase, each assigned to one spin species. However, it was found [1] that above certain magnetic fields, the two sets of  $h/e$  oscillations locked exactly in antiphase with no difference in amplitude, leaving apparently pure  $h/2e$  oscillations. These  $h/2e$  oscillations can be also observed [1] when the antidot gate voltage is swept at a fixed magnetic field.

The experimental results in Fig. 12 reveal an important feature of the  $h/2e$  oscillations. The data show the Aharonov-Bohm oscillations as the constrictions on either side of the antidot are squeezed by making the side-gate voltages more negative. In the top three curves, the antidot filling factor is  $\nu_c \sim 2$  and the oscillations have period  $h/2e$ , while in the bottom curve, where  $\nu_c < 1$ ,  $h/e$  oscillations appear. The fifth and sixth curves from the top do not exhibit any Aharonov-Bohm oscillations, except for very small peaks with period  $h/e$  above the  $\nu_c = 1$  plateau at the low- $B$  end. In the case of the bottom curve, the  $h/e$  oscillations clearly come from back-scattering through the antidot states with spin up (1-1 in the notation of Sec. 3.2).

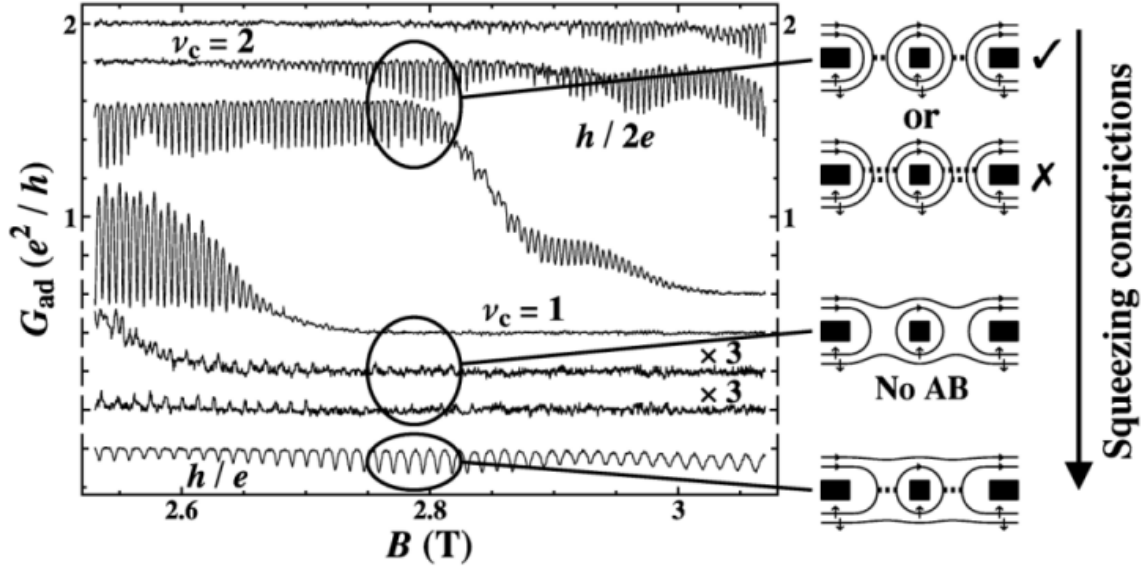


Fig. 12. Left:  $h/2e$  Aharonov-Bohm oscillations for the antidot with  $\nu_c = 2$  in the regime of magnetic fields  $B \sim 2.6 - 3$  T. Two curves are expanded by a factor of 3, as indicated. Right: Schematic diagrams of antidot states and extended edge channels (both are represented as solid lines) corresponding to the cases of different constriction widths shown in the left panel. Black dots indicate surface gates while the dotted lines represent the tunneling between the antidot and the extended edge channels. From Ref. [23].

As the constrictions are made wider, the  $h/e$  oscillations stop as the spin-up antidot states become decoupled from the extended edge channels that propagate through the constrictions (fifth and sixth curves). Then, when the constrictions are made even wider and the tunneling distance between the spin-up antidot state and spin-up extended edge channels becomes larger, there is no natural explanation why the back-scattering through the spin-up states should recover. This means that for  $h/2e$  Aharonov-Bohm oscillations, tunneling is only through antidot states with down spin, which have larger Zeeman energy than spin-up states.

Indeed, in later experiments using selective injection and detection of spin-resolved edge channels [26], it was confirmed that the antidot states with up spin do not provide resonant paths in the  $h/2e$  Aharonov-Bohm oscillations. The selective injection and detection can be used to distinguish the source of the resonance scattering, because the equilibration length of parallel-propagating edge channels can be extremely long [72,73] (longer than 1 mm depending on the conditions) especially at high magnetic fields, when the spatial overlap between the channels is small. In Ref. [26], as

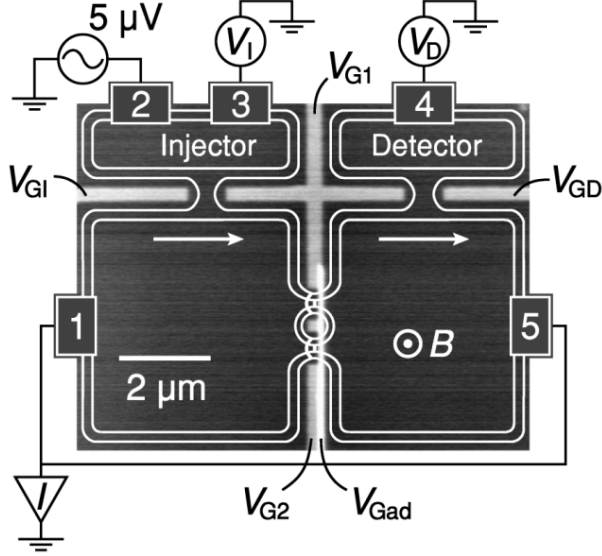


Fig. 13. Schematics of the measurement circuit for the spin-injection and detection experiment. Metal gates directly on the GaAs surface are seen in grey, and the second metal layer (on the cross-linked PMMA) is seen in bright white. Edge states in the case of  $\nu_I = \nu_D = 1$  and  $\nu_c = 2$  are shown as white lines. The arrows show the direction of electron flow. From Ref. [26].

shown in Fig. 13, split gates are used to control the current injection and detection of spin-resolved edge channels by controlling the filling factors  $\nu_I$  and  $\nu_D$  of the injector and the detector, respectively.

The effect of the selective injection and detection can be observed in the detector nonequilibrium conductance defined as

$$G_D = \frac{I}{V_D} = \nu_I \frac{e^2}{h} \frac{V_I}{V_D}. \quad (21)$$

Here,  $I = \nu_I(e^2/h)V_I$  is the current flowing through the injector constriction, and  $V_I$  and  $V_D$  are the voltages measured at the 2DEGs behind the injector and detector constrictions, respectively. We consider the particular case where the detector constriction is narrower than the injector (i.e.  $\nu_I \geq \nu_D$ ). If there is no scattering from the injected edge channels to other non-injected edge channels (the injected edge channels maintain the potential  $V_I$ ), the 2DEG region behind the detector constriction charges up to  $V_I$  (i.e.  $V_D = V_I$ ), as there is no drain contact here and the poten-

tials of all incoming edge channels are  $V_I$ . Therefore,  $G_D = G_I$  is expected, where  $G_I = I/V_I = \nu_I e^2/h$  is the injector two-terminal conductance. On the other hand, if inter-edge-state scattering occurs, the potential of the injected edge channels is lower than  $V_I$  at the detector constriction, and therefore  $V_D < V_I$  and  $G_D > G_I$ . Similarly, if back-scattering via antidot states (instead of inter-edge-state scattering) occurs from the injected edge channels, the edge channels lose their potential, resulting in  $G_D > G_I$ .

By this method, the spin states involved in antidot resonances can be detected. Figure 14(a) shows  $h/2e$  Aharonov-Bohm oscillations in the antidot conductance, and Figs. 14(b) and (c) show the nonequilibrium detector conductance with  $\nu_I = \nu_D = 2$  and  $\nu_I = \nu_D = 1$ , respectively. When both spin states are injected and detected [Fig. 14(b)], the shape of the  $h/2e$  oscillations that appear in  $G_D$  resembles that in  $G_{ad}$  (only mirror imaged). On the other hand, when only the spin-up edge channel is injected and detected, such oscillations are not observed. This provides direct evidence that, for pure  $h/2e$  Aharonov-Bohm oscillations, the resonance occurs only through the spin-down states (2-2 tunneling in the notation of Sec. 3.2).

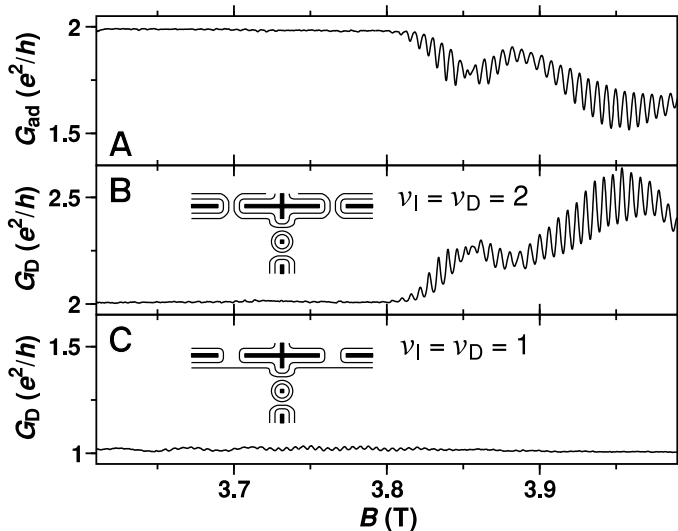


Fig. 14. (a)  $G_{ad}$  showing  $h/2e$  Aharonov-Bohm oscillations. (b) Detector conductance  $G_D$  with  $\nu_I = \nu_D = 2$  and (c) with  $\nu_I = \nu_D = 1$ . The facts that  $G_D$  in (b) mirrors  $G_{ad}$  almost perfectly and that oscillations are absent in (c) imply that only the spin-down edge channel of the lowest Landau level is involved in the resonant back-scattering process. From Ref. [26].

The  $h/2e$  oscillations of spin-down states cannot be understood from the noninter-

acting model described in Sec. 2.1. In the noninteracting model, the  $h/2e$  oscillations should be a simple composition of the two  $h/e$  oscillations coming from the two spin species, and the phase shift between the two  $h/e$  oscillations is determined by the ratio between the Zeeman energy and the single-particle level spacing (see Fig. 2). Since the ratio depends on the antidot potential around the Fermi level and the magnetic field, the noninteracting model cannot provide an explanation of the sample-independent feature, namely the  $\pi$  phase shift. Moreover, in the absence of interactions, both spins should participate in the resonant scattering, which is ruled out by the experimental observation that only the spin species with the larger Zeeman energy contributes to the resonances. Thus, it is necessary to have a model taking electron interactions into account. The formation of compressible rings around the antidot [23] was suggested to explain the  $h/2e$  oscillations. Later, a more generalized model was introduced [49], considering capacitive interactions between excess charges. We will review these models in Secs. 3.7 and 4.3, respectively.

Concluding this section, we note that the  $h/2e$  oscillations are not the full story of  $\nu_c = 2$  antidots. We will see in Sec. 3.8 that the Kondo effect [25] can also occur in  $\nu_c = 2$  antidots when the magnetic field is not as strong as in Fig. 12. An explanation for the antidot Kondo effect using the capacitive interaction model appears in Sec. 4.4.

### 3.5 *Spectator modes in antidot molecules*

In the previous section, we have seen that electron interactions can strongly affect the period of Aharonov-Bohm scattering. Similar behavior has been found [28] experimentally in an antidot molecule, a system of two coupled antidots. When the antidot molecule has both the “molecular” orbitals circulating the whole molecule and the “atomic” orbitals formed along each antidot, the Aharonov-Bohm scattering by the molecule exhibits only the peaks or dips with the period corresponding to the size of the atomic orbitals, and the molecular orbitals seem not to participate in the resonant scattering, *i.e.*, the molecular orbitals behave as “spectator” modes. We will discuss this behavior in this section.

Figure 15 shows a schematic view of the antidot molecule. In Ref. [28], two antidots of diameter  $0.2\ \mu\text{m}$  are fabricated symmetrically across the width of a long wide channel. The width of the narrow constriction between the two antidots is  $0.2\ \mu\text{m}$ . The antidot molecule has two spin-unresolved edge states coming from the lowest

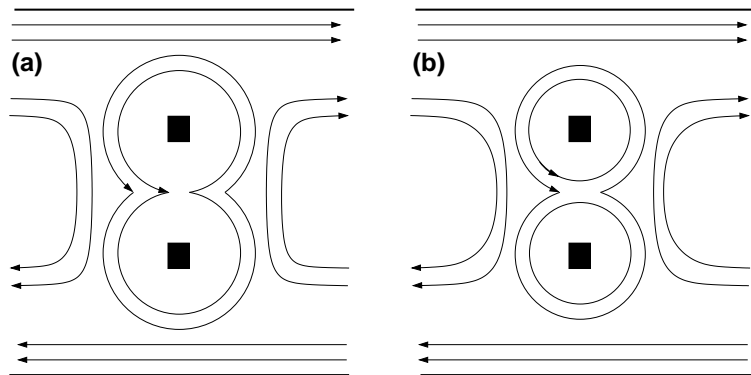


Fig. 15. Schematic diagrams of a  $\nu_c = 4$  antidot molecule. The central two black squares indicate the antidot gates, and the lines with arrows are the edge states. The antidot molecule consists of two antidots and it has two spin-unresolved edge states coming from the lowest two Landau levels. (a) All the states near the Fermi level have “molecular” character when the two antidots strongly couple to each other. (b) When the two antidots couple less strongly, the outer states coming from the second lowest Landau levels remain as molecular states while the inner states from the lowest Landau levels become “atomic” states localized at one of the antidots.

two Landau levels, *i.e.*,  $\nu_c = 4$ . By tuning two independent antidot gate voltages, one can continuously transform the states of the antidot molecule from those having “molecular” character to those having “atomic” nature. For example, when the two antidots strongly couple to each other, electrons cannot pass the constriction between the two antidots, and all the edge states circulate around both the antidots, having molecular character, as shown in Fig. 15(a). On the other hand, when the two antidots are tuned to couple less strongly, the outer states coming from the second lowest Landau level keep their molecular nature while the inner states from the lowest Landau level become atomic states circulating around only one of the two antidots.

The nature of the states of the two antidots was studied by observing the Aharonov-Bohm oscillations at fields below 1 T. In the case shown in Fig. 15(a), the period of the Aharonov-Bohm scattering was found to be consistent with the value estimated from the total size of the two antidots [see Fig. 16(a)]. So one can conclude that the molecular states contribute to the Aharonov-Bohm oscillations, as expected from a noninteracting model. However, such a simple story cannot describe experimental observations in the case of Fig. 15(b), where the antidot molecule has both the outer molecular orbitals circulating the whole molecule and the inner atomic orbitals formed along each antidot. One might expect from a noninteracting model that Aharonov-Bohm scattering has two possible periods, one corresponding to the

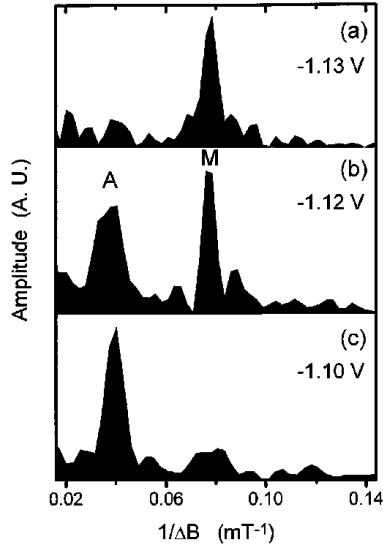


Fig. 16. Fourier transforms of the Aharonov-Bohm oscillations for the cases (a) that only molecular orbitals are formed, (b) that the antidot gate voltage is adjusted just above the center constriction’s pinch-off gate voltage, and (c) that both molecular and atomic orbitals are formed. Surprisingly, in (c), only the periodicity corresponding to the atomic orbitals are shown. From [28].

total size of the molecule and the other to the size of a single antidot, because the antidot molecule has both types of states. Or else, only molecular modes might be observed if the inner atomic modes are decoupled from the extended edge channels. However, surprisingly, only the periodicity corresponding to the atomic modes was found experimentally [see Fig. 16(c)]; both of the two periods exist over an extremely narrow range of antidot gate voltage just above the center constriction’s pinch-off gate voltage [see Fig. 16(b)]. This indicates that the outer molecular orbitals seem not to participate in the resonances.

Two different directions of understanding this “spectator” behavior of the outer molecular orbitals were proposed. One is to consider disorder that would destroy the resonances coming from the molecular orbitals [74], while the other is to consider Coulomb interactions [28]. We will briefly note the possible effect of Coulomb interactions on the molecular orbitals in Sec. 3.7. More studies are required to understand the mechanism of the spectator behavior of the molecular orbitals, for example to confirm the observation in more than one device.



### 3.6 Line shape of Aharonov-Bohm resonances

In the previous two sections, we have seen possible signatures of Coulomb interactions in the Aharonov-Bohm period. Another signature of Coulomb interactions has been also experimentally observed in the line shape of the resonant scattering by Maasilta and Goldman [21]. In the observation, the temperature dependence of a single Aharonov-Bohm resonance peak was analyzed in the regime of  $\nu_c = 1$  and  $1/3$  to determine the coupling parameter  $\alpha_{\text{coup}}$  between the antidot gate voltage and the energy of antidot bound states at the Fermi level. The behavior of  $\alpha_{\text{coup}}$  cannot be understood within the noninteracting approach in Sec. 2. The study of the line shape has been extended [24] to question the presence of the formation of compressible regions around the antidot at  $\nu_c = 2$  (see Sec. 3.7). In this section, we will describe the study of the line shape of a single resonance in the regime of integer  $\nu_c$ .

We first briefly summarize possible temperature dependences of the line shape of a resonance in various parameter regimes of temperature  $k_B T$ , resonance level spacing  $\Delta E$ , and level broadening  $\Gamma \equiv (\Gamma_L + \Gamma_R)/2$ , following Ref. [24]. Here, the resonant states are located between two (left and right) reservoirs, and their coupling energies to the reservoirs are  $\Gamma_L$  and  $\Gamma_R$ . In the Coulomb-blockade regime with  $\Gamma, \Delta E \ll k_B T$ , tunneling occurs through many resonant states around energy  $\epsilon_0$ , resulting in the line shape [75,76] of

$$G_T = G_p \frac{(\mu - \epsilon_0)/k_B T}{\sinh[(\mu - \epsilon_0)/k_B T]}, \quad G_p = \frac{e^2}{h} \frac{\rho \Gamma_L \Gamma_R}{2\Gamma}, \quad (22)$$

if the density of states  $\rho$  is constant. On the other hand, for  $\Gamma, k_B T \ll \Delta E$ , only one resonant state with energy  $\epsilon_0$  contributes to the line shape [77,32]. In the case of  $\Gamma \ll k_B T \ll \Delta E$ , thermal broadening governs the line shape as

$$G_T = G_p \cosh^{-2}\left(\frac{\mu - \epsilon_0}{2k_B T}\right), \quad G_p = \frac{e^2}{h} \frac{\pi \Gamma_L \Gamma_R}{4k_B T \Gamma}, \quad (23)$$

while in the case of  $k_B T \ll \Gamma \ll \Delta E$  one has the Breit-Wigner Lorentzian line shape,

$$G_T = \frac{e^2}{h} \frac{\Gamma_L \Gamma_R}{(\mu - \epsilon_0)^2 + \Gamma^2}. \quad (24)$$

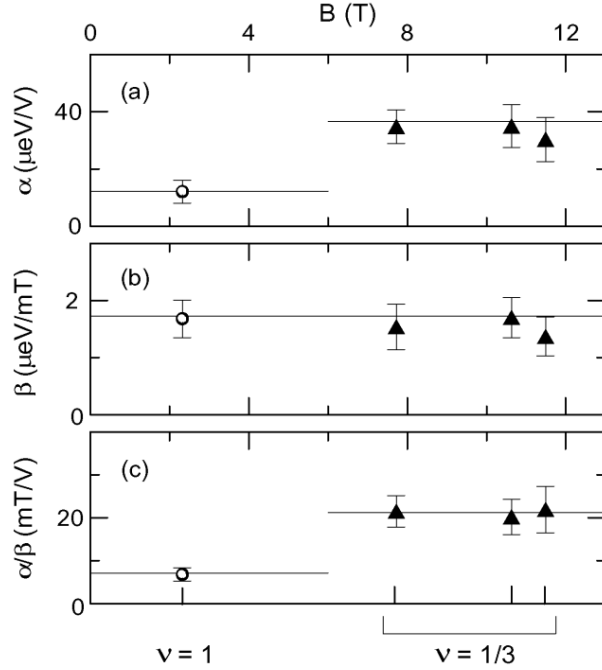


Fig. 17. (a) The coupling parameters  $\alpha_{\text{coup}}$ , (b)  $\beta_{\text{coup}}$ , and (c) their ratio are shown as a function of magnetic field. Both the cases of  $\nu_c = 1$  and  $\nu_c = 1/3$  are investigated. From Ref [21].

In the work [21] by Maasilta and Goldman, a single resonance peak was analyzed as a function of the magnetic field  $B$  or of the voltage  $V_{\text{BG}}$  on a large gate on the back of the sample. At all measurement temperatures, all the resonant Aharonov-Bohm peaks were found to fit the thermally broadened Fermi-Dirac line shape in Eq. (23) very well. The line shape of  $G_T \propto \cosh^{-2}[\alpha_{\text{coup}}(V_{\text{BG}}^m - V_{\text{BG}})/(2k_B T)]$  or  $G_T \propto \cosh^{-2}[\beta_{\text{coup}}(B^m - B)/(2k_B T)]$  was used, depending on whether  $V_{\text{BG}}$  or  $B$  varies. Here, the coupling parameters are introduced as

$$\alpha_{\text{coup}} \equiv |d(E_m - \mu)/dV_{\text{BG}}|, \quad (25)$$

$$\beta_{\text{coup}} \equiv |d(E_m - \mu)/dB|, \quad (26)$$

$E_m$  is the energy of the  $m$ -th resonance state, and  $V_{\text{BG}}^m$  and  $B^m$  are the positions of the  $m$ -th peak in gate voltage and magnetic field, respectively.

As shown in Fig. 17, the coupling parameter was found to have a constant value of  $\alpha_{\text{coup}, \nu_c=1} = 12 \pm 4 \mu\text{eV}/\text{V}$  in the regime of  $\nu_c = 1$ , whatever the field at which this

was chosen to occur. Surprisingly, this value is very similar to the value of  $\alpha_{\text{coup},B=0} = d\mu/dV_{\text{BG}}$  obtained in the model of two-dimensional electrons at zero magnetic field. Moreover, it has also a simple relationship with the value observed in the  $\nu_c = 1/3$  regime as  $\alpha_{\text{coup},\nu_c=1/3} \simeq 3\alpha_{\text{coup},\nu_c=1}$ . As a result, the addition energy  $\Delta E_{\text{tot}}$ , which can be obtained from the coupling parameters and the Aharonov-Bohm period in gate voltage ( $\Delta V_{\text{BG}}$ ) or in magnetic field ( $\Delta B$ ) via  $\Delta E_{\text{tot}} = \alpha_{\text{coup},\nu_c=1}\Delta V_{\text{BG}} = \beta_{\text{coup},\nu_c=1}\Delta B$ , has an almost constant value for a wide range of  $B$ . This constant value of  $\Delta E_{\text{tot}}$  cannot be understood in a noninteracting model, in which one may expect  $\Delta E_{\text{tot}} \sim 1/B$  [see Eq. (5)]. Maasilta and Goldman suggested that the constant  $\Delta E_{\text{tot}}$  arises from electron interactions in the self-consistent electrostatics of the quantum Hall edges. Interestingly, a similar result was found in the antidot charge detection experiment [22] as explained in Sec. 3.3. In Ref. [22], the constant  $\Delta E_{\text{tot}}$  was explained as coincidental cancellation in the  $B$  dependence of the charging energy and the single-particle level spacing. The observation of constant  $\Delta E_{\text{tot}}$  indicates that Coulomb interactions are important in the structure of antidot states.

### 3.7 Compressible regions around antidots

Along the extended edges of quantum Hall systems, strips of compressible regions, where the in-plane electric field can be screened, are considered to form where Landau levels intersect the Fermi level [54,55,56,57]. This has been confirmed by experiments in bulk 2DEGs (for example, see Ref. [78]). One may therefore question whether similar edge reconstruction causes the formation of compressible regions around an antidot, since an antidot provides an edge region of a quantum Hall system although the length of the antidot edge is finite. In this section, we will discuss whether the formation of compressible regions around an antidot is compatible with existing experimental observations, and introduce recent experimental efforts [23,24,58,59,61] of searching for compressible regions around an antidot.

Compressible regions formed along extended quantum Hall edges consist of partially filled states, so there is a continuous density of states around the Fermi level. One might consider that in the case of antidots this feature is incompatible with the experimental observation of discrete Aharonov-Bohm conductance resonances, because the discrete resonances require states to pass the Fermi energy one by one, *i.e.*, a discrete density of states. However, the introduction of the charging effect discussed in Sec. 3.3 removes the requirement of a discrete density of states for observing discrete resonances—resonant tunneling only occurs once per period, when the net

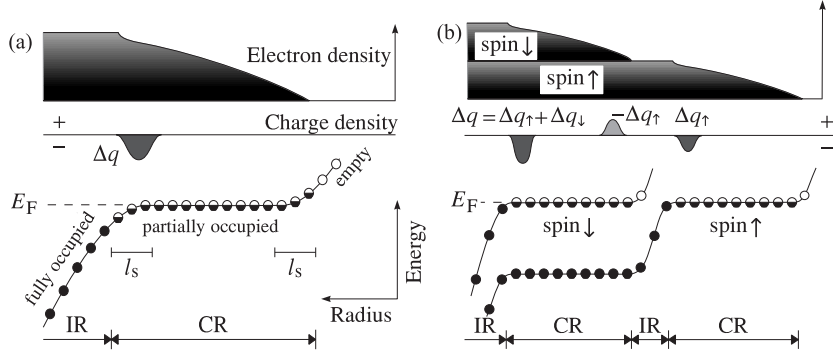


Fig. 18. Schematic diagrams of electron densities and energy-level structures around an antidot in the cases of (a)  $\nu_c = 1$  and (b)  $\nu_c = 2$  where compressible regions are assumed to be formed. In (b), the two spin branches of the lowest Landau levels form two compressible regions (CRs) separated by one incompressible region (IR). The outer compressible region tries to screen excess charge  $\Delta q_\uparrow$  of the inner spin-up compressible region, therefore,  $-\Delta q_\uparrow$  piles up at the inner edge of the outer compressible region in the case of perfect screening. As a result, the net charge  $\Delta q = \Delta q_\uparrow + \Delta q_\downarrow$  built up at the outer edge of the outer compressible region is the sum of the charging of both spins. Modified from Ref. [23].

charge around the antidot is  $\pm e/2$ , so that there is no energy cost for tunneling. Then the screening property of compressible regions can give the key to a heuristic picture for understanding electron interactions in antidots, as we will see below in a compressible-ring model.

The model with compressible rings around a  $\nu_c = 2$  antidot was suggested [23] to explain the  $h/2e$  Aharonov-Bohm oscillations. In this model, two compressible rings, *i.e.*, spin-up and down rings, are assumed to form around the antidot, although it is not clear [23,24,58,59,60,61] whether such compressible regions can be formed for the size of experimentally fabricated antidots; we will return to this issue later in this section. In both the compressible rings, a net excess charge accumulates as the magnetic field increases, as shown in Fig. 18(b). The incompressible ring formed between the two compressible rings acts as an insulating barrier, so that the two compressible regions form a capacitor. This capacitor mediates the interactions between the excess charges accumulated at the inner ring and those at the outer ring. Note that this interaction depends on the screening nature of the compressible rings (at least the outer one) and the environment of the antidot. Thus in the outer edge of the outer compressible ring, the total excess charge, coming from the two compressible rings, can pile up, and its relaxation period satisfies  $\Delta B = \phi_0/(2S) = h/(2eS)$ , resulting in  $h/2e$  oscillations that arise from tunneling through the spin-

down states only (“2–2” tunneling). This is in good agreement with the experimental observations shown in Figs. 12 and 14.

Another way of looking at this model is to consider the outer compressible region as a conducting cylinder (to the extent that electric field lines from the inner compressible ring terminate on the outer one rather than extending to the gates ten times further away). Increasing the magnetic field “pumps” charge into the region bounded by the (insulating) incompressible strip outside this cylinder, at a rate of  $e$  per  $h/e$  of flux increase, for *each* of the spin-up and down Landau levels. By Gauss’s Law, it is irrelevant what happens inside the conducting cylinder. The extra charge must appear on the outer edge of the cylinder, so it accumulates at a rate of  $e$  per  $h/2e$ . Thus every time the flux increases by  $h/2e$ , an electron can leave, and so there are tunneling resonances, as for conventional Coulomb-blockade, with period  $h/2e$ , and hence “double-frequency” oscillations are observed. In Fig. 18(b),  $\Delta q_{\downarrow}$  is the change in charge in the outer compressible region, but it is interesting to realize that this is not purely caused by extra spin-down charge. In fact, though the charge in the spin-up Landau level mainly goes into the inner ring (as  $\Delta q_{\uparrow}$ ), the remainder serves to increase the electron density in that spin’s incompressible states in the region of the other spin’s compressible region (filled circles in that region in Fig. 18(b)).

We note, firstly, that this model really only requires a compressible outer ring, so the inner one may be incompressible (as found in recent calculations [60], see Sec. 4.6) and secondly, that the model was later generalized [49] into a capacitive interaction model without the assumption of compressible regions as such (see Sec. 4.3).

This compressible-ring model might also give a clue to understanding the spectator modes observed in antidot molecules discussed in Sec. 3.5. Excess charges accumulated in the inner atomic orbital region can be screened by the outer molecular orbitals. Then, the total excess charge piled up in the outer orbital region comes from both the outer and the inner regions, and the relaxation of the total excess charge does not necessarily have the resonance period corresponding to the total size of the antidot molecule, though it seems unlikely that it would have the required (atomic) periodicity. Also, the excitation spectra observed in Fig. 11 imply that compressible regions do not form at low fields below about 2 T. More studies are required to understand the mechanism of the spectator behavior.

Although the compressible-ring model may be useful in understanding certain experimental observations, it has been controversial whether compressible regions really form around antidots, or if so under what conditions. Karakurt and coworkers stud-

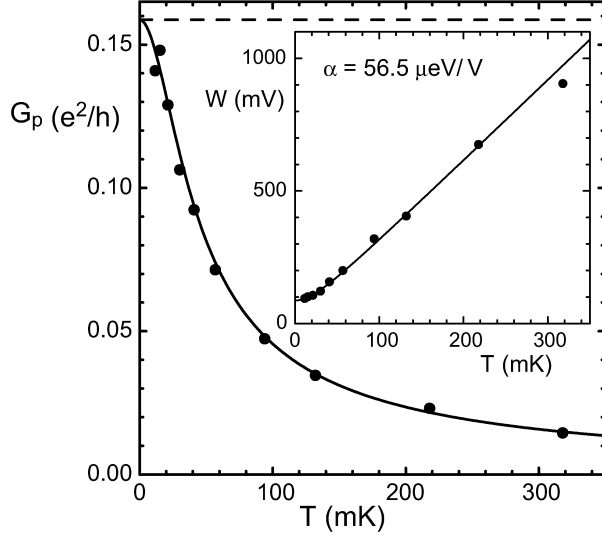


Fig. 19. Peak tunneling conductance  $G_p$  as a function of temperature  $T$ .  $G_p$  is obtained by fitting line shapes of measured peaks to  $G_T = G_p \cosh^{-2}[(V_{G,AD0} - V_{G,AD})/W]$ , which comes from Eq. (23). For temperatures  $35 \text{ mK} < T < 320 \text{ mK}$ ,  $G_p \propto 1/T$  (solid curve). Inset: The dependence of the width parameter [see Eq. (25)]. For  $T > 35 \text{ mK}$ ,  $W \propto T$ . From Ref. [24].

ied the line shape of resonant peaks in the regime of  $\nu_c = 2$  in order to understand the antidot state structure [24]. The radius of the measured antidot was estimated as  $0.34 \mu\text{m}$  from the Aharonov-Bohm period, and the range of magnetic field investigated was around  $B \sim 1 \text{ T}$  in the  $\nu_c = 2$  regime. To see any possible signature of the formation of compressible regions around a  $\nu_c = 2$  antidot, the measured line shape was fitted by the two curves in Eqs. (22) and (23). Over the range of temperature,  $35 \text{ mK} < T < 320 \text{ mK}$ ,  $G_p$  was found to follow  $G_p \sim 1/T$  (see Fig. 19), indicating that Eq. (23) provides a better fit. This means that the resonant tunneling mechanism through the antidot is different from the simple resonance model in the regime of  $\Gamma, \Delta E \ll k_B T$ , where a  $T$ -independent  $G_p$  is expected. Based on this observation and on the fact that there should exist many partially filled single-particle states in compressible regions [54,55,56,57], Karakurt and his coworkers concluded that there is no compressible region around the studied antidot.

However, this conclusion was questioned [58,59]. The assumption made by Karakurt *et al.* was that the simple resonance model with a large number of states within  $k_B T$  should describe the temperature dependence of tunneling via a compressible region. The  $T$ -independent  $G_p$  of the line shape in Eq. (22) is derived based on

the assumption that the density of states is constant over a range wider than  $k_B T$ . This is unlikely to be the case in compressible regions, where the density of states is expected to have a peak at the Fermi level. Calculations [79] suggest that the width of the peak in the density of states is of the order of  $k_B T$  and is therefore temperature-dependent. In such a case, Eq. (22) is not applicable, and the  $1/T$  dependence measured by Karakurt *et al.* is expected for  $G_p$ , assuming that the width of the compressible region, and hence the number of states through which tunneling occurs, are independent of  $T$ .

In addition, one may easily expect the formation of compressible regions to be strongly dependent on magnetic field, antidot size, electron density, etc. Therefore, the absence of compressible regions in one experimental regime may not mean their absence in another. Compressible regions were invoked by Kataoka *et al.* in order to explain “double-frequency” oscillations [1,2,23,26] at  $B \sim 3$  T, three times higher than the range investigated in Ref. [24].

Michael *et al.* investigated the single-particle energy spacing  $\delta\epsilon$  and the charging energy, both deduced from the excitation spectrum, as a function of  $B$  ( $B < 2$  T) [61]. It was found that  $\delta\epsilon$  decreased faster than the expected  $1/B$  dependence. No excitation spectrum has been observed in the “pure double-frequency” regime at higher fields, where the compressible model describes the system well [23]. This may be evidence that the antidot potential flattens, forming compressible regions, as the magnetic field increases. However, in the experiments, the antidot potential is not circularly symmetric because of side constrictions. The bulging of the states in the constrictions can also lead to a similar deviation from the  $1/B$  behavior of  $\delta\epsilon$  as the edge states are reflected from the constriction [80], though whether this fully explains the behavior of  $\delta\epsilon$  is not yet clear; the data in Ref. [61] were mainly taken on resonant transmission peaks above the  $\nu_c = 2$  plateau, where the effect of the edge-state reflection from the constriction is expected to be weak. Complete understanding of this regime still remains elusive.

In order to investigate the possibility of antidot compressible regions from the theoretical side, Ihnatsenka and Zozoulenko recently reported [60], based on spin density-functional theory, that the formation mechanism of the compressible regions around an antidot is very different from the case of extended edges [56,57], and that the exchange interaction is very important in the case of  $\nu_c = 2$ . This theoretical work will be discussed in Sec. 4.6. Further systematic experimental and theoretical studies on the formation of compressible regions around an antidot are required, and such studies should be valuable in understanding local disorder regions in the integer

quantum Hall regime.

### 3.8 Kondo-like zero-bias anomaly

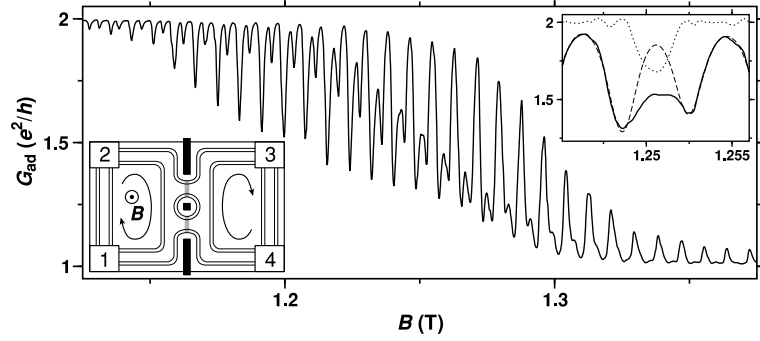


Fig. 20. Antidot conductance  $G_{\text{ad}}$  at a lattice temperature of 25 mK as a function of the magnetic field  $B$  in the transition region between the  $\nu_c = 2$  and 1 plateaus. Top-right inset: The fitting of a pair of dips around  $B = 1.25$  T by using four dips proportional to the Fermi-function derivative. The solid curve is the experimental result, while the dashed line is the fit. The dotted line shows the difference between the experimental curve and the fit (offset by  $2e^2/h$ ). Bottom-left inset: Schematic view of the measured antidot geometry, which is identical to the setup in Fig. 3. The numbered rectangles on the corners represent Ohmic contacts. From Ref. [25].

The Kondo effect is one of the most well-studied many-body phenomena. It arises from the interactions between a localized electron spin and many free electrons [81,82]. Recently, there has been renewed interest in the effect, as it was predicted [62,83] and observed [84,85,86,87] in quantum dots. The localized spin arises naturally in a quantum dot, when the dot is in the Coulomb-blockade regime and contains an odd number of electrons. The experimental tunability of the parameters of quantum dots enables the study of the Kondo effect in great detail. In Sec. 3.3, we saw some similarities between a quantum dot and an antidot in the integer quantum Hall regime, such as Coulomb blockade. However, despite the similarities, one may not expect the Kondo effect in antidots because of the large Zeeman splitting and hence the lack of apparent spin degeneracy. In fact, in a  $\nu_c = 2$  antidot, Kondo-like behavior in the conductance of an antidot has been observed experimentally, with no Zeeman splitting as a function of DC bias. We note that Kondo behavior in strong magnetic fields has also been observed in a quantum dot [88], and attributed to an unpaired electron at the edge of the dot that arises periodically as electrons are redistributed



between the center and the edge, but this does show the expected Zeeman splitting in DC bias. Therefore, the mechanism behind the antidot Kondo effect must be different from the cases of quantum dots. In this section, we will review the experimental observation of the Kondo-like behavior, while the theoretical model for the effect will be discussed in Sec. 4.4.

Figure 20 shows typical behavior of the conductance  $G_{\text{ad}}$  of an antidot (see also Fig. 3) in the transition regime between  $\nu_c = 2$  and  $\nu_c = 1$ . The effective antidot radius is estimated from the measured Aharonov-Bohm period as  $r_{\text{AD}} \sim 0.36 - 0.40 \mu\text{m}$ , depending on the antidot gate voltage, and the bulk filling factor is  $\nu_{\text{bulk}} \simeq 10$ . At low magnetic field  $B$  where  $G_{\text{ad}}$  is close to the  $\nu_c = 2$  quantum Hall plateau value of  $2e^2/h$ , one can see that there are two conductance dips in one Aharonov-Bohm period  $\Delta B = h/(eS)$ . As  $B$  increases, the coupling between the antidot and the extended edge channels becomes stronger, since the edge states move towards the center of the antidot constriction. As a result, the amplitude of the dips increases. At the same time, two neighboring dips become paired and eventually unrecognizable as two independent dips about 1.3 T as  $G_{\text{ad}}$  approaches the  $\nu_c = 1$  plateau value of  $e^2/h$ . Very similar features were observed between the  $\nu_c = 2$  and  $\nu_c = 1$  plateaus with different gate voltages and with different magnetic fields from 0.8 to 1.5 T. At magnetic fields above 3 T, the pairing of the dips disappears, and instead pure  $h/2e$  Aharonov-Bohm oscillations appear.

The pairing was analyzed by using a fit based on the Fermi-function derivative. As shown in the inset of Fig. 20, such a simple fit cannot reproduce the observed data. The fit shows that there seems to be another dip in the intra-pair gap, resulting in a large discrepancy in that region. This extra dip cannot be explained by the noninteracting model in Sec. 2, in which there are only two dips within the  $B$  range of one Aharonov-Bohm period.

The extra dip has the following features. Firstly, it is absent in a magnetic field larger than 3 T. Secondly, when a small source-drain dc bias  $V_{\text{sd}}$ , even as small as  $15 \mu\text{V}$ , is applied, the extra dip vanishes, leaving two well-defined dips, as shown in Fig. 21(a). The Coulomb-diamond structures of dark lines arise at large bias  $V_{\text{sd}}$  in Fig. 21(b), indicating the two well-defined dips. Note that from the height of the diamond, the charging energy can be estimated to be  $\sim 60 \mu\text{eV}$ . Thirdly, the extra dip becomes stronger as  $B$  increases [see Fig. 21(b) and 21(c)]. We note that the coupling between the antidot and the extended edge channels increases in stronger  $B$ . Fourthly, the extra dip becomes suppressed as the temperature  $T$  increases, as shown in Fig. 22. At  $T \sim 190 \text{ mK}$ , the extra dip is almost absent. The amplitude of the extra dip

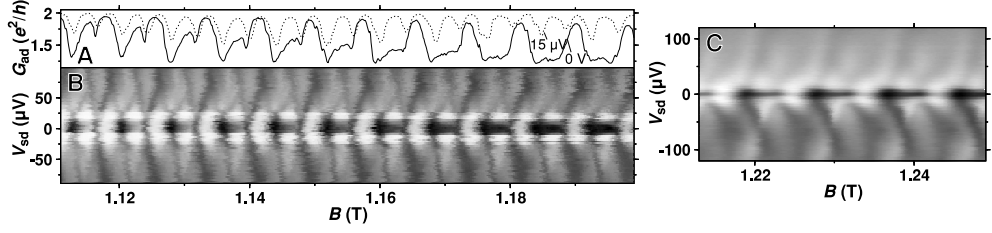


Fig. 21. The dependence of  $G_{\text{ad}}$  on source-drain bias voltage  $V_{\text{sd}}$ . (a)  $G_{\text{ad}}$  vs  $B$  at 25 mK with  $V_{\text{sd}} = 0$  V (solid line) and with  $V_{\text{sd}} = 15 \mu\text{V}$  (dashed). (b) Gray-scale plot of the differential conductance  $G_{\text{ad}}$  against  $B$  and  $V_{\text{ad}}$  (white:  $2e^2/h$ , black:  $1.2e^2/h$ ). The horizontal dark lines along  $V_{\text{ad}} = 0$  show the extra dip (see text). (c) Similar gray-scale plot to (b) in the regime of stronger coupling between the antidot and the extended edge channels (white:  $1.8e^2/h$ , black:  $1.1e^2/h$ ). From Ref. [25].

decreases monotonically as  $T$  increases.

The above bias and temperature dependences of the extra dip are strikingly similar to those of the Kondo effect in quantum dots (although the zero-bias anomaly persists over too small a range of temperatures for a logarithmic temperature dependence, which is the hallmark of the Kondo effect, to be discernible). Moreover, stronger coupling normally enhances the Kondo features, which is also in good agreement with the above dependence of the extra dip on the coupling. The observation of the antidot Kondo effect may not be surprising, based on the similarities between quantum dots and antidots. On the other hand, a counter-argument would be that the Kondo effect cannot occur, because the antidot has considerable Zeeman splitting of  $E_Z = 30 \mu\text{eV}$  at  $B = 1.2$  T. The width of the observed zero-bias anomaly of  $\sim 20 \mu\text{eV}$  implies that any splitting in bias can be at most about one-third of the expected Zeeman splitting at that field. We will see in Sec. 4.4, based on a capacitive interaction model, that the  $\nu_c = 2$  antidot can indeed show this antidot Kondo effect.

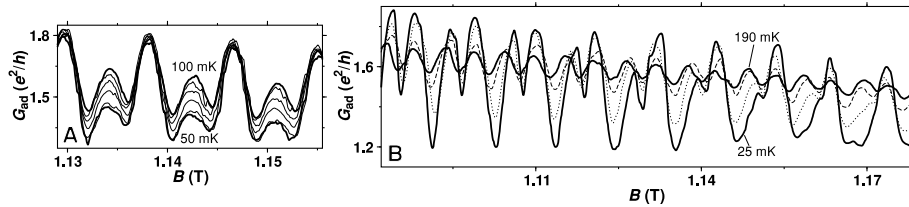


Fig. 22. (a) Temperature dependence of  $G_{\text{ad}}$  vs  $B$  with small increments of temperature  $\sim 10$  mK. (b) The same as (a), but representative traces from a wider range of  $T$ . From Ref. [25].

## 4 Theoretical studies on electron interactions in antidots

The experimental observations discussed in the previous sections indicate that electron-electron interactions may play an important role in an antidot in the integer quantum Hall regime. To theoretically treat electron interactions in a general situation, one can either construct a phenomenological model Hamiltonian or numerically solve a full many-body Hamiltonian using some approximations. The former way is powerful in the sense that it can provide simple understanding and basic physics of the system of interest, but it relies on a few phenomenological parameters. On the other hand, the latter can provide the justification of the former way and predict many-body ground states, but it requires intensive numerical calculations. The two approaches are complementary to each other. The effects of electron interactions in an integer quantum Hall antidot have been studied in both ways.

The first theoretical treatment of electron interactions in an integer quantum Hall antidot was reported only recently [49]. It provides a phenomenological model for a  $\nu_c = 2$  antidot, based on capacitive interactions of excess charges localized around the antidot. This model is similar to the capacitive-interaction model for a quantum dot [5,6,50], and it may explain the key features of the nontrivial Aharonov-Bohm oscillations accompanied by the antidot charging effect, the  $h/2e$  Aharonov-Bohm oscillations, and the antidot Kondo effect discussed in Secs. 3.3, 3.4, and 3.8, respectively. This phenomenological model has been tested [49,52] by a Hartree-Fock numerical study. The Hartree-Fock calculation has shown that a maximum-density droplet of holes can be the ground state of an antidot in some parameter regimes, and that the transitions of the droplet ground states can be well described by the capacitive-interaction model. A numerical calculation based on spin density-functional theory has also been performed [60] very recently, to investigate the formation of compressible regions around an antidot. This study shows that the widths of the compressible regions can be narrower than those of compressible regions formed along the extended edges of a quantum Hall system, and finds that exchange interactions can suppress the formation of some of the possible compressible regions.

In this section, we review the above theoretical works on electron interactions in an integer quantum Hall antidot. It includes the total Hamiltonian of the antidot (Sec. 4.1), the origin of excess charges (Sec. 4.2), the capacitive-interaction model for a  $\nu_c = 2$  antidot and its description of the  $h/2e$  oscillations (Sec. 4.3), an explanation of the antidot Kondo effect based on the capacitive-interaction model (Sec. 4.4), the Hartree-Fock study and the prediction of a hole maximum-density droplet (Sec. 4.5),

and the spin density-functional study of compressible regions around antidots (Sec. 4.6).

#### 4.1 Total Hamiltonian

We consider the antidot system shown in Fig. 3. A strong perpendicular magnetic field ( $B > 1$  T) is applied so that the system is in the integer quantum Hall regime with bulk filling factor  $\nu_{\text{bulk}}$ . The antidot local filling factor is chosen to be  $\nu_c = 1$  or 2 ( $\nu_c \leq \nu_{\text{bulk}}$ ) for comparison with experiments. In this case, antidot states come only from the two spin-split branches of the lowest Landau level; we assume that the Landau-level mixing from the higher Landau levels may be neglected due to the strong magnetic field even in the presence of electron interactions. It is assumed that the localized antidot states and the extended edge channels are tunnel-coupled, and that the period of the Aharonov-Bohm oscillations is much smaller than the strength of the applied magnetic field,  $\Delta B = h/(eS) \ll B$ . This condition is achieved when the effective antidot area  $S$  is large enough or when  $B$  is sufficiently strong. This is a key assumption of the capacitive-interaction model for an antidot, as will be discussed in Secs. 4.2 and 4.3, because it allows one to have a sufficiently slowly varying antidot potential  $V_{\text{AD}}(r)$  within the scale of the magnetic length  $l_B$ .

The total Hamiltonian of the system can be written as

$$H_{\text{tot}} = H_{\text{AD}} + H_{\text{edge}} + H_{\text{tun}}. \quad (27)$$

The Hamiltonian  $H_{\text{AD}}$  for the antidot states is

$$H_{\text{AD}} = \sum_{m\sigma} \epsilon_{m\sigma} c_{m\sigma}^\dagger c_{m\sigma} + \frac{1}{2} \sum_{mm'nn'\sigma\sigma'} W_{mm'nn'} c_{m\sigma}^\dagger c_{m'\sigma'}^\dagger c_{n'\sigma'} c_{n\sigma}, \quad (28)$$

where  $c_{m\sigma}^\dagger$  creates an electron with spin  $\sigma$  in the localized single-particle state enclosing  $m$  magnetic flux quanta,  $\epsilon_{m\sigma}$  is the single-particle energy, and  $W$  is the Coulomb interaction. The single-particle energy  $\epsilon_{m\sigma} = \hbar\omega_c/2 + \epsilon_\sigma^Z + V_{\text{AD}}(m)$  comes from the lowest Landau-level energy  $\hbar\omega_c/2$ , Zeeman energy  $\epsilon_\sigma^Z$ , and the antidot potential energy  $V_{\text{AD}}$ . The antidot potential energy is governed by the antidot gate voltage and includes the positive background term preserving total charge neutrality. The Hamiltonian  $H_{\text{edge}}$  of the extended edge channels is written as

$$H_{\text{edge}} = \sum_{ik\sigma} \epsilon_{ik\sigma} c_{ik\sigma}^\dagger c_{ik\sigma}, \quad (29)$$

where  $c_{ik\sigma}^\dagger$  creates an electron in the extended edge state with momentum  $k$ , energy  $\epsilon_{ik\sigma}$ , spin  $\sigma$ , and Landau-level index  $i$ . Note that electron interactions of the extended edge channels are neglected in this regime of integer filling factor  $\nu_c$ . The extended edge channels can tunnel-couple to antidot states through incompressible quantum Hall regions in between with coupling strength tuned by the side and antidot gate voltages. The tunneling Hamiltonian  $H_{\text{tun}}$  is written as

$$H_{\text{tun}} = \sum_{ikm\sigma} V_{km\sigma}^i c_{ik\sigma}^\dagger c_{m\sigma} + \text{H.c.} \quad (30)$$

We only consider the extended edge channels coming from the first and the second Landau levels ( $i \in \{a, a', b, b'\}$ ) [see Fig. 3], since the extended edge channels of higher Landau levels have smaller and negligible tunneling amplitudes  $V_{km\sigma}^i$  to antidot states.

## 4.2 Derivation of excess charge

In the capacitive-interaction model for antidots, the antidot Hamiltonian  $H_{\text{AD}}$  in Eq. (28) can be simply described by the capacitive coupling of excess charges formed around the antidot. In this section, we provide the origin of the excess charge and derive its dependence on magnetic field  $B$  for a large-size antidot.

We first sketch the origin and typical behavior of the excess charge. A many-body state of an antidot can be constructed by single-particle antidot states discussed in Sec. 2, which are phase-coherent closed orbits encircling the antidot. The  $m$ -th single-particle state encloses an integer number  $m$  of magnetic flux quanta,  $m = BS_m/\phi_0$ , where  $S_m$  is the area enclosed. As  $B$  adiabatically increases by  $\delta B (< \Delta B)$ , each single-particle state moves with respect to the antidot potential  $V_{\text{AD}}(r)$  by  $\Delta r_m \sim -\sqrt{S_m} \delta B/B$ , adjusting the enclosed area in order to keep the flux  $BS_m$  constant. Thus the position of electron density of the many-body state moves towards the center of the antidot. Since the positive background charge does not move at all at the same time, this displacement of electron density results in charge imbalance around the antidot, *i.e.*, continuous accumulation of local excess charge (see Fig. 10) [1,22]. In this way, the variation of magnetic field  $B$  modifies the excess charge of the

antidot, and thus it acts like a gate voltage for a quantum dot.

The accumulated excess charge relaxes via resonant tunneling. The relaxation is a discrete event because of the insulating incompressible regions between the excess charge and extended edge channels, and it can be observed as a resonant peak or dip in tunneling conductance  $G_{\text{ad}}$ , depending on the nature of its coupling to the extended edge channels, as discussed in Secs. 2.2 and 3.1. Note that in the fractional quantum Hall regimes, the relaxation may be accompanied by fractional charge tunneling [89].

Below, we derive the magnetic-field dependence of the excess charge  $\delta q_\sigma$ . For simplicity, we first consider a  $\nu_c = 1$  antidot. The extension of the derivation to the case of  $\nu_c = 2$  is straightforward, as we will see later.

To see the behavior of the excess charge as a function of magnetic field  $B$ , one may start with a constant-interaction model. In the constant-interaction model for a quantum dot [5,6,50], electron interactions are described by an effective capacitive interaction. It works well in the case where the dot is almost isolated, so that the number of electrons within the dot can be treated as a good quantum number. The effective capacitive interaction is modeled by a set of capacitances, which are treated as constant within a narrow range of gate voltage applied to the dot. One can adopt a similar strategy for the antidot when it weakly couples to extended edge channels only via tunneling through the incompressible regions in between. For a given magnetic field  $B_0$  and a fixed antidot gate voltage, a part of the antidot Hamiltonian  $H_{\text{AD}}$  in Eq. (28), which includes the antidot potential  $V_{\text{AD}}(m)$  and the electron-electron interaction  $W_{mm'nn'}$  terms, can be approximately described by an effective capacitive interaction,

$$E_{\text{AD}}^{\nu_c=1}(B_0) = \frac{(N^{\text{AD}}e - Q_G(B_0))^2}{2C}. \quad (31)$$

Here,  $C$  is an effective antidot capacitance,  $N^{\text{AD}}$  is the total number of electrons occupying the single-particle antidot states, and  $Q_G$  is the positive “antidot gate charge” governed by the antidot gate voltage. The spin index  $\sigma$  is dropped in this case of  $\nu_c = 1$ . As an antidot is an open system,  $N^{\text{AD}}$  may not be a well-defined quantity. However, a strict definition of  $N^{\text{AD}}$  is not necessary here, as one can see below. The important property of  $N^{\text{AD}}$  is that it can vary only by an integer number due to charge discreteness. On the other hand, the antidot gate charge  $Q_G$  can vary continuously. This leads to Coulomb-blockade oscillations as a function of the antidot gate voltage. We note that the contribution from the single-particle energies (due to

a rising antidot potential), the single-particle level spacing, can be absorbed into the capacitive energy in Eq. (31) [37], either if  $N^{\text{AD}}$  is large or if the single-particle energy levels can be approximated to follow a linear function of angular momentum  $m$  with a constant level spacing, as described below.

As  $B$  varies from  $B_0$  by  $\delta B$  ( $< \Delta B \ll B_0$ ), the position  $r_m$  of the single-particle state enclosing  $m$  magnetic flux quanta is shifted by  $\delta r_m$  with respect to the antidot potential  $V_{\text{AD}}(r)$ , resulting in the energy variation of the state  $\delta\epsilon_m = dV_{\text{AD}}(r)/dr|_{r=r_m}\delta r_m$ , since the amount of flux enclosed by each single-particle state is preserved. This preservation,  $\delta(B\pi r_m^2) = 0$ , gives  $\delta r_m = -(r_m/2B_0)\delta B$ , so  $\delta\epsilon_m$  can be approximated as a linear function of  $\delta B$  when  $V_{\text{AD}}(r)$  varies slowly on the scale of the magnetic length  $l_B(\equiv \sqrt{\hbar}/eB)$  and is locally linear in  $r$ . The energy shift coming from the variations of the cyclotron and Zeeman energies is also linear in  $\delta B$ , and thus can be absorbed into  $\delta\epsilon_m$ . By introducing the average value  $\overline{\delta\epsilon_m}$  of  $\delta\epsilon_m$  for occupied single-particle states, one can find the shift of total single-particle energy  $\delta E(\delta B) = N^{\text{AD}}\overline{\delta\epsilon_m}$ . The shift can be rewritten in terms of a function  $Q_B(\delta B) \equiv -C\overline{\delta\epsilon_m}(\delta B)/e$  as

$$\delta E(\delta B) = -eN^{\text{AD}}Q_B(\delta B)/C. \quad (32)$$

Notice that  $Q_B(\delta B)$  is a linear function of  $\delta B$  when  $dV_{\text{AD}}(r)/dr$  can be assumed to be constant as in a large-size antidot. By summing this single-particle energy shift and the capacitive interaction in Eq. (31), one can arrive at the dependence of the total energy of the antidot on  $\delta B$ :

$$\begin{aligned} E_{\text{AD}}^{\nu_c=1}(B_0 + \delta B) &= \frac{(N^{\text{AD}}e - Q_G(B_0) - Q_B(\delta B))^2}{2C} + E_{\text{AD},0}^{\nu_c=1} \\ &= \frac{\delta q^2}{2C} + E_{\text{AD},0}^{\nu_c=1}, \end{aligned} \quad (33)$$

where  $E_{\text{AD},0}^{\nu_c=1}$  is a term independent of  $N^{\text{AD}}$  (the dependence of  $E_{\text{AD},0}^{\nu_c=1}$  on  $N^{\text{AD}}$  may be ignored under the assumption of large  $N^{\text{AD}}$  or constant  $\delta\epsilon_m$ ). From this expression, one can interpret  $Q_B$  as an ‘‘antidot magnetic-gate charge’’, and  $\delta q$  as an excess charge given by

$$\delta q = N^{\text{AD}}e - Q_G(B_0) - Q_B(\delta B). \quad (34)$$

This expression shows that the excess charge  $\delta q$  varies with magnetic field. The

magnetic-field dependence of  $\delta q$  can be also derived [36,37] in a field-theoretical language with the action  $\delta\mathcal{L} = \vec{j} \cdot \vec{A}$ , where  $\vec{j}$  is the current density along the antidot circumference and  $A$  is the vector potential. The control of the excess charge near an antidot by using magnetic field is reminiscent of the charge control by a gate voltage in a quantum dot.

By using the form of the effective energy in Eq. (33), one can study the Coulomb blockade by a large-size  $\nu_c = 1$  antidot. The antidot magnetic-gate charge  $Q_B(\delta B)$  has a real value, similarly to  $Q_G$ , thus one has Coulomb-blockade oscillations of  $N^{\text{AD}}$  or  $\delta q$  as a function of magnetic field. Relaxation of  $\delta q$  is allowed whenever

$$E_{\text{AD}}^{\nu_c=1}(\delta q \pm e) = E_{\text{AD}}^{\nu_c=1}(\delta q), \quad (35)$$

which is satisfied by  $\delta q = \pm e/2$ . We remark that the energy in Eq. (33) and the condition (35) can provide a good description for the charging and relaxation behavior of  $\nu_c = 1$  antidots (see Sec. 3.3) studied experimentally in Ref. [22]. Note that the energy in Eq. (33) does not include the contribution from neutral excitations [37], which have the energy gap of the single-particle level spacing in the noninteracting limit. Therefore, the condition (35) is valid at bias and temperature lower than the neutral-excitation energy.

To understand the periodic nature of  $\delta q(B)$ , we may imagine the simple situation where the electron density around an antidot is only shifted without any charge redistribution. This situation can be achieved only when an incompressible region or a maximum-density droplet of holes [52] (see Sec. 4.5) is formed around an antidot. In this case, one can estimate  $\delta q = -2\pi en_e r \delta r$  for the change  $\delta B \equiv B - B_0$  ( $\Delta B \ll B$ ), where  $r$  is the effective antidot radius,  $\delta r$  is the shift caused by  $\delta B$ , and  $n_e$  is the electron density. Since  $\delta(B\pi r^2) = 0$  and the density can be expressed as  $n_e = eB/h$  in the  $\nu_c = 1$  regime, one can find a simple but intuitive dependence of  $\delta q$  on magnetic field  $B$ ,

$$\delta q(B) \sim -\Delta Q_B(B) \sim -e(B - B_0)/\Delta B. \quad (36)$$

Therefore, the amount of accumulation of  $\delta q$  in one Aharonov-Bohm period  $\Delta B$  is one electron charge  $e$  in the  $\nu_c = 1$  regime. This accumulation is combined with the relaxation, giving rising to the expected result that  $\delta q$  has the same periodicity as the Aharonov-Bohm oscillations. When one takes the redistribution of electron density into account,  $\delta q$  may be approximated to be a linear function of  $B$  for a



large-size antidot with potential varying smoothly over several magnetic lengths. In this case, the accumulation and relaxation of  $\delta q$  are expected still to be periodic. This periodic nature of the  $B$ -dependent evolution of the excess charge is consistent with the experimental findings in the  $\nu_c = 1$  regime [22] (see Sec. 3.3).

The extension of the above derivation to the  $\nu_c = 2$  case is straightforward. In this case, one can introduce spin-dependent excess charges,  $\delta q_\uparrow$  and  $\delta q_\downarrow$ , coming from the spin-split branches of the lowest Landau level, and a two-by-two capacitance matrix (with spin index  $\sigma$ ) is required to describe the capacitive interactions between the excess charges; the detailed form of the model Hamiltonian will be introduced in Eq. (39) in Sec. 4.3. By generalizing Eq. (34), one can use an expression for  $\delta q_\sigma$

$$\delta q_\sigma = eN_\sigma^{\text{AD}} - Q_{G\sigma} - Q_{B\sigma}(B), \quad (37)$$

where  $N_\sigma^{\text{AD}}$ ,  $Q_{G\sigma}$ , and  $Q_{B\sigma}(B)$  are the spin-dependent occupation number, antidot gate charge, and antidot magnetic-gate charge, respectively. When the antidot potential varies linearly within the scale of magnetic length  $l_B$ , one may use an approximate linear form,

$$Q_{B\sigma}(B) + Q_{G\sigma} = e(a_\sigma B + b_\sigma), \quad (38)$$

between two adjacent relaxation events of  $(\delta q_\uparrow, \delta q_\downarrow)$  within a sufficiently small range of magnetic field, as in the above  $\nu_c = 1$  case. Here,  $a_\sigma e$  is the rate of excess charge accumulation with increasing  $B$ ,  $a_\sigma > 0$ , and  $b_\sigma e$  originates from the positive background charge. From the discussion around Eq. (36), one has  $a_\sigma \simeq 1/\Delta B_\sigma = S_\sigma/\phi_0$ , where  $S_\sigma$  is the effective area enclosed by  $\delta q_\sigma$ . When  $S \simeq S_\sigma \gg S_\uparrow - S_\downarrow$ , one has  $a_\uparrow \simeq a_\downarrow \simeq S/\phi_0$ . Note that a recent Hartree-Fock numerical calculation [52] has shown the behavior of excess charge to be consistent with the linear form in Eq. (38), which will be discussed in Sec. 4.5.

In the  $\nu_c = 2$  case, the evolution of excess charges,  $(\delta q_\uparrow, \delta q_\downarrow)$ , as a function of magnetic field is not as simple as in the  $\nu_c = 1$  case, because of the interactions between  $\delta q_\uparrow$  and  $\delta q_\downarrow$ . As will be shown in the next two sections, the capacitive interaction between  $\delta q_\uparrow$  and  $\delta q_\downarrow$  leads to a characteristic evolution of  $(\delta q_\uparrow, \delta q_\downarrow)$  which can explain the  $h/2e$  Aharonov-Bohm oscillations and the Kondo effect discussed in Secs. 3.4 and 3.8.

### 4.3 Capacitive interaction model for $\nu_c = 2$ antidots

In this section, we introduce the capacitive interaction model Hamiltonian for a  $\nu_c = 2$  antidot, and discuss the accumulation and relaxation of excess charges  $(\delta q_\uparrow, \delta q_\downarrow)$  as a function of magnetic field  $B$  [49]. Various sequences of single-particle normal resonant relaxations and Kondo-type resonant relaxations can appear in the evolution of  $(\delta q_\uparrow, \delta q_\downarrow)$ , depending on the interaction strength between  $\delta q_\uparrow$  and  $\delta q_\downarrow$  and the spin-dependent effective antidot area  $S_\sigma$ .

In the  $\nu_c = 2$  case, the localized excess charges  $\delta q_\uparrow$  and  $\delta q_\downarrow$  are spatially separated from each other and from extended edge channels by insulating incompressible regions. This feature allows us to describe the antidot Hamiltonian (28) by using capacitive coupling of excess charges. By generalizing the model Hamiltonian for the  $\nu_c = 1$  antidot in Eq. (33), one can write the total energy  $E_{\text{AD}}^{\nu_c=2}(B)$  of a  $\nu_c = 2$  antidot as

$$E_{\text{AD}}^{\nu_c=2}(\delta q_\uparrow(B), \delta q_\downarrow(B)) = \frac{1}{2} \sum_{\sigma\sigma'} \delta q_\sigma (C^{-1})_{\sigma\sigma'} \delta q_{\sigma'}. \quad (39)$$

Here,  $\delta q_\sigma$  has the form in Eq. (37) and the effective capacitance matrix  $C_{\sigma\sigma'}$  is written as

$$C^{-1} = \begin{pmatrix} (C^{-1})_{\uparrow\uparrow} & (C^{-1})_{\uparrow\downarrow} \\ (C^{-1})_{\downarrow\uparrow} & (C^{-1})_{\downarrow\downarrow} \end{pmatrix} = \frac{1}{C_{\uparrow\uparrow}C_{\downarrow\downarrow} - C_{\uparrow\downarrow}^2} \begin{pmatrix} C_{\downarrow\downarrow} & -C_{\uparrow\downarrow} \\ -C_{\uparrow\downarrow} & C_{\uparrow\uparrow} \end{pmatrix}. \quad (40)$$

$C_{\sigma\sigma'}$  is a classical electrostatic quantity if alternating compressible and incompressible regions [56,57] are formed around the antidot, while it is a phenomenological parameter in other cases. One has  $C_{\uparrow\uparrow} < C_{\downarrow\downarrow}$ , since  $\delta q_\downarrow$  is located further away from the center of the antidot than  $\delta q_\uparrow$  due to its higher Zeeman energy. In addition,  $C_{\uparrow\downarrow} < 0$  and  $|C_{\uparrow\downarrow}|$  is the smallest among  $C_{\sigma\sigma'}$ , as it is a mutual capacitance. Note that the cyclotron energy and the Zeeman energy are counted in the definitions of  $\delta q_\sigma$  and  $C$ , as they also cause the displacement and the separation of each  $\delta q_\sigma$ .

For large antidots with  $B \gg \Delta B$ ,  $\delta q_\sigma(B)$  in Eqs. (37, 38) and  $E_{\text{AD}}$  in Eq. (39) can provide a good model describing the Coulomb blockade and charge relaxations of a  $\nu_c = 2$  antidot, as in the capacitive interaction model for the  $\nu_c = 1$  case (see Sec. 4.2). Moreover, since  $C_{\sigma\sigma'}$  varies only slightly within one Aharonov-Bohm period,

one can take it as constant; in this case, the dependence of  $E_{\text{AD}}^{\nu_c=2}$  on  $B$  is governed only by  $\delta q_\sigma(B)$ . The validity of the capacitive interaction model in Eqs. (37, 38, 39) has been tested [52] using a Hartree-Fock approach (see Sec. 4.5). This test shows that the transition of a hole maximum-density-droplet ground state of an antidot can be described well by the model.

When antidot states weakly couple to extended edge channels, Coulomb blockade prohibits the relaxation of  $(\delta q_\uparrow, \delta q_\downarrow)$  unless one of the following conditions is satisfied. First, a normal resonance occurs whenever  $E_{\text{AD}}^{\nu_c=2}$  is invariant under single-electron tunneling [see Eq. (35) for  $\nu_c = 1$ ], i.e.,

$$E_{\text{AD}}^{\nu_c=2}(\delta q_\uparrow, \delta q_\downarrow) = E_{\text{AD}}^{\nu_c=2}(\delta q_\uparrow \pm e, \delta q_\downarrow), \quad (41)$$

or

$$E_{\text{AD}}^{\nu_c=2}(\delta q_\uparrow, \delta q_\downarrow) = E_{\text{AD}}^{\nu_c=2}(\delta q_\uparrow, \delta q_\downarrow \pm e). \quad (42)$$

Another process can occur via spin-flip cotunneling, in which an electron tunnels into an antidot state and another electron with the opposite spin tunnels out via a virtual state or vice versa. The condition for this is

$$E_{\text{AD}}^{\nu_c=2}(\delta q_\uparrow, \delta q_\downarrow) = E_{\text{AD}}^{\nu_c=2}(\delta q_\uparrow \pm e, \delta q_\downarrow \mp e). \quad (43)$$

Among many available virtual states, the one with the lowest energy (thus with the biggest contribution) is either  $(\delta q_\uparrow \pm e, \delta q_\downarrow)$  or  $(\delta q_\uparrow, \delta q_\downarrow \mp e)$ . The cotunneling process, combined with other spin-nonflip cotunneling, can give rise to a Kondo resonance, which will be described in Sec. 4.4. We call Eq. (43) as Kondo resonance condition hereafter.

By combining the resonant relaxation conditions and the accumulations of excess charge one can study the evolution of  $(\delta q_\uparrow, \delta q_\downarrow)$  as a function of magnetic field  $B$ . As discussed before in Sec. 4.2, the accumulation of  $\delta q_\sigma$  may be approximated as a linear function of  $\delta q_\sigma = -e(a_\sigma B + b_\sigma)$  [see Eq. (38)] between two adjacent relaxation events, assuming that the antidot potential  $V_{\text{AD}}(r)$  varies linearly within the scale of magnetic length  $l_B$  and  $\Delta B \ll B$ . The two important parameters governing the evolution of excess charges are the ratio of accumulation rates  $a_\uparrow/a_\downarrow$  and the ratio of capacitances  $\alpha \equiv |C_{\uparrow\downarrow}|/C_{\uparrow\uparrow}$ , as we will see below.

To follow the evolution of excess charges, it is useful to draw the trajectories of

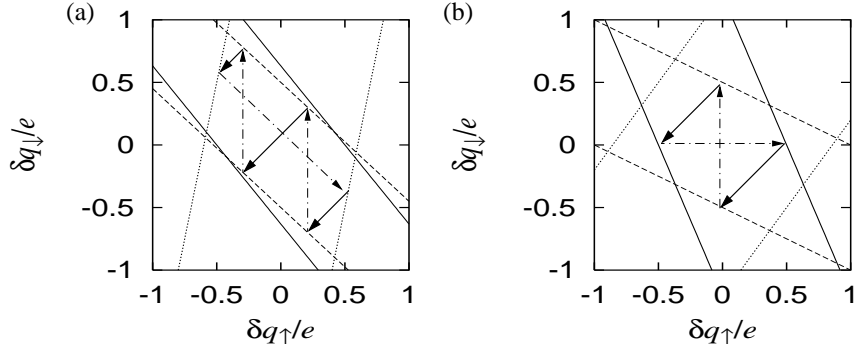


Fig. 23. Evolution of the excess charges  $(\delta q_{\uparrow}, \delta q_{\downarrow})$  as a function of magnetic field  $B$  in the case of  $S_{\uparrow} = S_{\downarrow}$ . The solid-arrow trajectories indicate the direction of the evolution with increasing  $B$ . When one of resonance conditions is met,  $(\delta q_{\uparrow}, \delta q_{\downarrow})$  jumps following horizontal (normal spin-up electron tunneling), vertical (normal spin-down electron tunneling), or diagonal dashed-dotted (Kondo resonance) arrows. Solid, dashed, and dotted lines indicate resonance conditions of Eqs. (41), (42), and (43), respectively, and they constitute the boundaries of a hexagonal cell, in which  $(\delta q_{\uparrow}, \delta q_{\downarrow})$  evolves. Two different parameters are used: (a)  $\alpha \equiv |C_{\uparrow\downarrow}|/C_{\uparrow\uparrow} = 0.95$  and (b) 0.5. For both the cases,  $C_{\downarrow\downarrow}/C_{\uparrow\uparrow} = 1.2$  is chosen. From Ref. [49].

evolution in a two-dimensional plane of  $(\delta q_{\uparrow}, \delta q_{\downarrow})$ , as shown in Fig. 23. As the accumulation of  $(\delta q_{\uparrow}, \delta q_{\downarrow})$  is determined by the rates  $a_{\uparrow}e$  and  $a_{\downarrow}e$  [see Eq. (38)], the evolution trajectory follows a line parallel to  $\delta q_{\uparrow} = (a_{\uparrow}/a_{\downarrow})\delta q_{\downarrow}$  with increasing  $B$ , until it jumps at one of the resonance conditions. Therefore, the evolution trajectory of  $(\delta q_{\uparrow}, \delta q_{\downarrow})$  is confined in a hexagonal cell, the boundaries of which are defined by the three resonance conditions in Eqs. (41, 42, 43). The trajectories (solid arrows in Fig. 23) parallel to the line of  $\delta q_{\uparrow} = (a_{\uparrow}/a_{\downarrow})\delta q_{\downarrow}$  mean the accumulation of excess charges, while their jumps (following dashed-dotted arrows) between the boundaries of the cell indicate one of the three possible resonant relaxations. The horizontal and vertical jumps correspond to the normal resonant tunneling of single electron with spin up and that of spin down [Eqs. (41) and (42)], respectively, while the diagonal jumps occur whenever the Kondo resonance condition [Eq. (43)] is satisfied.

Now one can see the dependence of the evolution trajectories, or of the sequence of resonant tunneling events, on the ratios  $a_{\uparrow}/a_{\downarrow}$  and  $\alpha \equiv |C_{\uparrow\downarrow}|/C_{\uparrow\uparrow}$ . We first consider the case of  $a_{\uparrow} \simeq a_{\downarrow}$ , which can appear when the spatial separation of  $\delta q_{\uparrow}$  and  $\delta q_{\downarrow}$  is small compared with their average radius, *i.e.*, when  $S_{\downarrow} - S_{\uparrow} \ll S_{\downarrow}$ . In this case, as  $B$  increases, the ground-state value of  $(\delta q_{\uparrow}, \delta q_{\downarrow})$  evolves parallel to the line of  $\delta q_{\uparrow} = \delta q_{\downarrow}$ . By using this fact, one can show geometrically very easily that the evolution

trajectory  $(\delta q_\uparrow, \delta q_\downarrow)$  is always closed in the hexagonal cell and periodic with period  $\Delta B = \phi_0/S$  in this case of  $a_\uparrow \simeq a_\downarrow$ .

In the case of  $a_\uparrow \simeq a_\downarrow$ , one can further notice that there are two possible types of evolution trajectory when  $C_{\uparrow\uparrow} < C_{\downarrow\downarrow}$ , depending on the parameter  $\alpha \equiv |C_{\uparrow\downarrow}|/C_{\uparrow\uparrow}$  and the initial value of  $(\delta q_\uparrow, \delta q_\downarrow)$  at a starting value of magnetic field. The first type (i) consists of two consecutive tunneling events of spin-down electrons as well as one intermediate Kondo resonance in one Aharonov-Bohm period  $\Delta B$  [see Fig. 23(a) and Fig. 24], while the other type (ii) is composed of alternating tunneling events of spin-up and down electrons with an arbitrary phase difference [Fig. 23(b) and Fig. 24]. In type (i), the tunneling of a spin-up electron, which is assumed to have smaller Zeeman energy, is *always* Coulomb blocked, while in type (ii), the sequence of resonant tunneling events shows two *independent* periodic events (each with Aharonov-Bohm period  $\Delta B$ ) of the normal spin-up and down resonances. If  $\alpha$  has the maximum value of  $\alpha = 1$ , all trajectories are of type (i) regardless of the initial value of  $\delta q_\sigma$ . In the other extreme case of  $\alpha = 0$  (minimum), i.e.,  $C_{\uparrow\downarrow} = 0$ , the two spin states are completely uncorrelated and all trajectories are of type (ii). For  $0 < \alpha < 1$ , both types are allowed depending on the initial values of the  $\delta q_\sigma$ . For larger  $\alpha$ , more trajectories follow type (i). One may notice that the type (i) trajectory itself depends on  $\alpha$ . In type (i), the difference in magnetic field between the two consecutive tunneling events of spin-down electrons within one Aharonov-Bohm period  $\Delta B$  is exactly  $\Delta B/2$  for  $\alpha = 1$  (maximum) while for smaller  $\alpha$  it starts to deviate from  $\Delta B/2$  to  $\Delta B/(1 + \alpha)$  or to  $\Delta B\alpha/(1 + \alpha)$ .

The experimental observations for  $\nu_c = 2$  antidots [1,2,23,25,26] are consistent with the type (i) trajectory at  $\alpha \simeq 1$ . In high magnetic fields around 3 T, they show the  $h/2e$  Aharonov-Bohm oscillations, i.e., evenly spaced resonance dips of antidot conductance that appear two times per  $\Delta B$  [1,2,23]. In lower magnetic fields around 1.2 T [25], another dip related to the Kondo resonance can appear approximately once every  $\Delta B$  at low temperatures below the Kondo temperature  $T_K$  (see Sec. 4.4), while the Kondo-related dips disappear and the  $h/2e$  Aharonov-Bohm oscillations emerge at high temperature. Moreover, a spin-resolved measurement [26] shows that only the electrons with spin down can contribute to the  $h/2e$  oscillations. Therefore, based on this agreement, one may argue that the experiments are in the parameter regime of  $\alpha \simeq 1$ , where the mutual Coulomb interactions between  $\delta q_\uparrow$  and  $\delta q_\downarrow$  are as strong as those characterized by the self capacitances  $C_{\uparrow\uparrow}$  or  $C_{\downarrow\downarrow}$ .

When the areas enclosed by  $\delta q_\uparrow$  and  $\delta q_\downarrow$  are different,  $S_\downarrow \neq S_\uparrow$ , the accumulation rate  $a_\sigma$  of excess charges is spin-dependent so that the ground-state value of  $(\delta q_\uparrow, \delta q_\downarrow)$

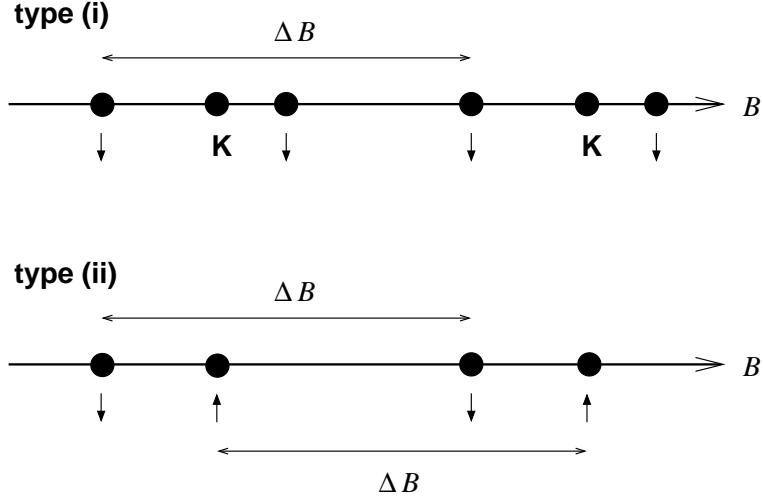


Fig. 24. Two types of possible sequence of relaxation events (filled circles) of  $(\delta q_\uparrow, \delta q_\downarrow)$  as a function of magnetic field  $B$  in the case of  $a_\uparrow \simeq a_\downarrow$ . The normal resonances of electrons with spin up, those with spin down, and Kondo resonances are marked by up arrow, down arrow, and the letter “K”, respectively. In the type (i) sequence, a pair of spin-down normal resonances periodically appears with Aharonov-Bohm period  $\Delta B$ , while Kondo resonances occur once within the pair in one  $\Delta B$ . The position of the Kondo resonances depends on the initial point of the evolution of  $(\delta q_\uparrow, \delta q_\downarrow)$ , and there exist no spin-up normal resonances for type (i). In the type (ii) sequence, spin-up and down normal resonances occur alternately, while there is no Kondo resonance. Each normal resonance appears periodically with period  $\Delta B$ .

evolves parallel to the line of  $\delta q_\uparrow = (a_\uparrow/a_\downarrow)\delta q_\downarrow$  with increasing  $B$ . The resulting trajectories depend on  $\alpha$  as in the above case of  $S_\downarrow = S_\uparrow$ . For  $\alpha = 1$ , as in type (i), all trajectories of  $(\delta q_\uparrow, \delta q_\downarrow)$  have resonant tunneling of spin-down electrons as well as Kondo tunneling, while they cannot have resonant tunneling of spin-up electrons due to Coulomb blockade. However, in contrast to type (i) resonances, they are not periodic, although each of their spin-down resonant-tunneling and Kondo tunneling events has its own periodicity ( $\Delta B_\downarrow$  and  $\Delta B_K$ , respectively). The relation between  $\Delta B_\downarrow$  and  $\Delta B_K$  is found to be  $\Delta B_K/\Delta B_\downarrow = 1 + a_\downarrow/a_\uparrow$ . For  $0 < \alpha < 1$ , the trajectory does not have a simple structure. All of spin-up resonant tunneling, spin-down resonant tunneling, and Kondo tunneling can appear in this case. For  $\alpha = 0$ , all trajectories consist of two independent periodic spin-up and down resonances (with period  $\Delta B_\uparrow = \phi_0/S_\uparrow$  and  $\Delta B_\downarrow = \phi_0/S_\downarrow$ , respectively), similar to type (ii), as easily expected.

#### 4.4 Antidot Kondo effect

In this section, we describe in detail how the Kondo effect can arise in the capacitive interaction model  $E_{\text{AD}}^{\nu_c=2}$  [Eq. (39)] for a  $\nu_c = 2$  antidot. We first introduce the mapping of  $E_{\text{AD}}^{\nu_c=2}$  to a Kondo Hamiltonian, discuss an effective Zeeman energy originated from the spin-dependent tunneling strength, which might suppress the Kondo resonance, and finally analyze the experimental observation of antidot conductance in the Kondo regime.

We first show the capacitive interaction model can be mapped into a Kondo impurity Hamiltonian, as in the cases of quantum dots [50]. In the vicinity of a Kondo resonance condition [Eq. (43)], only the two lowest  $[(\delta q_\uparrow, \delta q_\downarrow)$  and  $(\delta q_\uparrow + e, \delta q_\downarrow - e)]$  and the next two excited states  $[(\delta q_\uparrow + e, \delta q_\downarrow)$  and  $(\delta q_\uparrow, \delta q_\downarrow - e)]$  among possible antidot states are important when the charging energy is strong enough. Thus one can ignore all the other excited states, which may affect the Kondo effect only slightly as in multilevel quantum dots [90,91]. Using these four lowest states one can map  $E_{\text{AD}}^{\nu_c=2}$  into the Anderson impurity model, given by a truncated Hamiltonian

$$H_{\text{imp}} = \sum_{\sigma} \epsilon_{\sigma} d_{\sigma}^{\dagger} d_{\sigma} + U d_{\uparrow}^{\dagger} d_{\downarrow}^{\dagger} d_{\downarrow} d_{\uparrow},$$

where  $d_{\sigma}^{\dagger}$  creates an electron in the impurity site. The two lowest states constitute the two singly occupied impurity states, while the next two excited states are the empty and doubly occupied states. Defining  $E_{\text{empty}} \equiv E_{\text{AD}}^{\nu_c=2}(\delta q_\uparrow + e, \delta q_\downarrow)$ , one can identify the energy levels of the Anderson impurity Hamiltonian as

$$\begin{aligned} \epsilon_{\uparrow} &= E_{\text{AD}}^{\nu_c=2}(\delta q_\uparrow, \delta q_\downarrow) - E_{\text{empty}}, \\ \epsilon_{\downarrow} &= E_{\text{AD}}^{\nu_c=2}(\delta q_\uparrow + e, \delta q_\downarrow - e) - E_{\text{empty}}, \\ U + \epsilon_{\uparrow} + \epsilon_{\downarrow} &= E_{\text{AD}}^{\nu_c=2}(\delta q_\uparrow, \delta q_\downarrow - e) - E_{\text{empty}}. \end{aligned}$$

One can find that the difference between  $\epsilon_{\uparrow}$  and  $\epsilon_{\downarrow}$  is zero only at the point where the Kondo resonance condition (43) is satisfied. As a result, the Anderson impurity site has an *effective* Zeeman energy of  $\Delta\epsilon \equiv \epsilon_{\uparrow} - \epsilon_{\downarrow}$  in the vicinity of the Kondo resonance points. Note that the real Zeeman energy splitting  $E_Z$  is irrelevant to the antidot Kondo effect, as the Zeeman energy can be absorbed in the definition of the excess charges, as discussed before. Now one can replace the total Hamiltonian

$H_{\text{tot}}$  in Eq. (27) with that of the Anderson impurity coupled to the extended edge channels by amplitude  $V_{k\sigma}^i$ :

$$H_K = H_{\text{imp}} + H_{\text{edge}} + \sum_{ik\sigma} V_{k\sigma}^i c_{ik\sigma}^\dagger d_\sigma + \text{H.c.} \quad (44)$$

The  $k$  dependence of  $V_{k\sigma}^i$  is usually ignored, for simplicity.

To see whether the Kondo effect can appear in real experimental situations, one needs to estimate energy scales from the experimental data (Ref. [25]). In the experiment of Ref. [25], the  $h/2e$  oscillations were recovered at high temperature (see Fig. 22), where the Kondo effect was suppressed. This indicates  $\alpha \simeq 1$  in the experimental situation, so one may focus on the type (i) trajectory with  $\alpha = 1$ . Since only spin-down electrons cause the normal resonances in the type (i) trajectories, one may rewrite Eq. (39) as

$$E_{\text{AD}}^{\nu_e=2}(\delta q_\uparrow, \delta q_\downarrow) = \frac{(\delta q_\downarrow + \alpha \delta q_\uparrow)^2}{2C_{\text{out}}} + \frac{\delta q_\uparrow^2}{2C_{\text{in}}}, \quad (45)$$

where  $C_{\text{out}} = C_{\downarrow\downarrow} - \alpha|C_{\uparrow\downarrow}|$  and  $C_{\text{in}} = C_{\uparrow\uparrow}$ . From this expression, one finds that  $e^2/C_{\text{out}}$  corresponds to the charging energy ( $\sim 60 \mu\text{eV}$ ) measured in Ref. [25], from which one can estimate  $-\epsilon_\sigma$  and  $U + \epsilon_\sigma$  based on energy relations of the Anderson impurity [82]  $-\epsilon_\sigma, U + \epsilon_\sigma \sim e^2/(2C_{\text{out}})$ . To estimate further  $e^2/C_{\text{in}}$ , one can use the following fact. In the experiment of Ref. [25], a Kondo dip appears only within a certain finite window  $\delta B$  of magnetic field in each Aharonov-Bohm period. The finite window may be related to the effective Zeeman energy  $\Delta\epsilon$ , which can split and suppress the Kondo resonance [92]. For  $\alpha = 1$ , the Kondo resonance occurs at  $\delta q_\uparrow = \pm e/2$  (where  $\Delta\epsilon = 0$ ), and in its vicinity where  $\delta q_\uparrow = \pm(1/2 - p)e$ , one finds  $\Delta\epsilon = pe^2/C_{\text{in}}$ . From this,  $e^2/C_{\text{in}}$  is roughly estimated to be of the order of  $10 \mu\text{eV}$  using the experimental results [25] of  $\Delta\epsilon \lesssim 10 \mu\text{eV}$  (the energy scale of the zero-bias anomaly), the width  $\delta B$  of a Kondo dip  $\simeq \Delta B/4$ , and  $p \simeq \delta B/\Delta B$ . By using the estimated energy scales and from a numerical renormalization-group calculation [93,94,82], the Kondo temperature was found [49] to be  $T_K \sim 1 \mu\text{eV}$ , which is similar to the energy scale of the zero-bias anomaly of the antidot Kondo effect [25].

One interesting point of the antidot setup in Fig. 3 is that the resonance width  $\Gamma_\sigma(E) \equiv \sum_i \Gamma_\sigma^i(E)$  has spin dependence since the distance between the antidot and the extended edge channel  $a$  (see Fig. 3) is spin dependent, *i.e.*,  $V_{k\uparrow}^{i=a(a')} \neq V_{k\downarrow}^{i=a(a')}$ ,



where  $\Gamma_\sigma^i(E) = 2\pi \sum_k |V_{k\sigma}^i|^2 \delta(E - \epsilon_{ik\sigma})$ . The spin-dependent  $\Gamma_\sigma$ 's renormalize the effective Zeeman energy as  $\Delta\tilde{\epsilon}(\delta q_\uparrow, \delta q_\downarrow)$ , as in quantum dots coupled to ferromagnetic leads [95,96]. This changes the Kondo resonance condition to

$$E_{\text{AD}}(\delta q_\uparrow \pm e, \delta q_\downarrow \mp e) = E_{\text{AD}}(\delta q_\uparrow, \delta q_\downarrow) + \Delta\tilde{\epsilon}, \quad (46)$$

instead of Eq. (43). When Eq. (46) is satisfied, there is no renormalized effective Zeeman splitting so that one can estimate [97]  $T_{\text{K}} \sim (\sqrt{\Gamma U}/2) \exp(\pi\epsilon(U + \epsilon)/\Gamma U)$ , where  $\Gamma = (\Gamma_\uparrow + \Gamma_\downarrow)/2$ .

It is worth pointing out that, at high magnetic fields  $B \sim 3$  T, the Kondo dips have not been found experimentally [23]. In this regime, the Kondo dips may be suppressed, leaving  $h/2e$  oscillations, since the spin-up antidot states are almost decoupled from all extended edge channels.

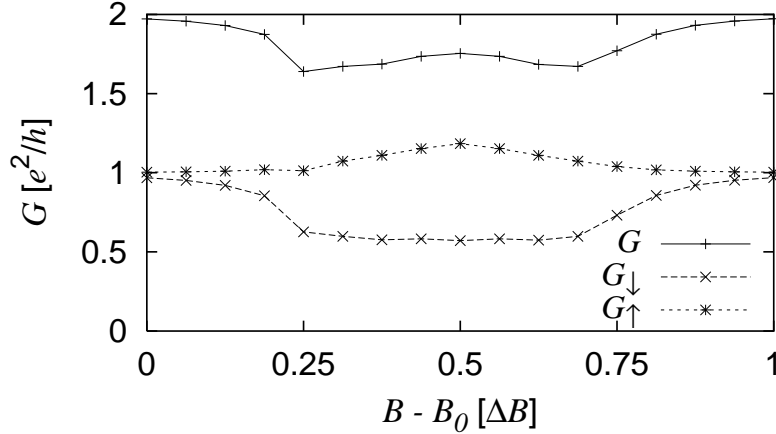


Fig. 25. Calculated antidot conductance  $G_{\text{ad}}(B)$  and its spin-dependent component  $G_\sigma(B)$  around a magnetic field  $B_0$  ( $\sim 1$  T).  $G_{\text{ad}}(B)$  matches well the experimental data in the inset of Fig. 20. This plot of  $G_{\text{ad}}(B)$  is obtained by solving the Hamiltonian  $H_{\text{K}}$  in Eq. (44) using the numerical renormalization-group method, and by applying the result into Eq. (15). In the calculation, the dependence of the coupling  $V_{k\sigma}^i$  on the channel index  $i$  and on  $\sigma$  is fully taken into account; the dependence of  $V_{k\sigma}^i$  on  $k$  is ignored and the extended edge channels are approximated to have infinite bandwidth, to see the low-energy limit. From Ref. [49].

Now we describe the line shape of the antidot Kondo effect (see the inset of Fig. 20). In Ref. [49], the line shape was calculated by using the zero-temperature expression of the antidot conductance  $G_{\text{ad}}$  (as well as that of its spin component  $T_\sigma$ ) derived in

Sec. 2.2 [see Eqs. (15) and (16)]. The parameters used in the conductance expression, the level broadening  $\Gamma_\sigma^i$ 's, can be estimated from Ref. [25] in the following way: since the experimental result of the antidot conductance  $G_{\text{ad}}(B)$  shows dips below  $2e^2/h$  [see Fig. 20] and the excess charges follow a type (i) trajectory, one can expect that the spin-down electrons favor *backward* scattering, *i.e.*,  $\Gamma_\downarrow^{i=a,a'} > \Gamma_\downarrow^{i=b,b'}$  and  $T_\downarrow < 0$ . On the other hand, the experimental result of the  $\Delta B$  periodic peaks at stronger magnetic fields near the plateau of  $G_{\text{ad}} \simeq e^2/h$  may be interpreted as normal resonances of spin-up electrons. Combined with the fact that  $\Gamma_\sigma^{i=a,a'}$  is smaller for weaker  $B$ , such an interpretation indicates that the spin-up electrons favor *forward* scattering, *i.e.*,  $\Gamma_\uparrow^{i=a,a'} < \Gamma_\uparrow^{i=b,b'}$  and  $T_\uparrow > 0$  (opposite to the case for spin down), for weaker  $B$  where  $G_{\text{ad}} > e^2/h$ . The type (i) trajectory with  $\alpha = 1$ , the above features of the level broadenings, and the calculation of  $\sin^2 \theta_\sigma$  based on a numerical renormalization group approach allow one to get the antidot conductance  $G_{\text{ad}}(B)$  for one Aharonov-Bohm period, as shown in Fig. 25. The result of  $G_{\text{ad}}(B)$  is in qualitatively good agreement with the experimental data in Fig. 20.

The spin-dependent component  $G_\sigma$  in Fig. 25 can be understood as follows.  $G_\uparrow$  has only one Kondo peak, while  $G_\downarrow$  shows a mixture of two normal and one intermediate Kondo resonance dips. As a result, at the center of the Kondo resonance, even if the unitary Kondo limit is reached,  $G_{\text{ad}}$  can be greater than  $e^2/h$ . The center and the width of the Kondo resonance are governed by Eq. (46) and  $e^2/C_{\text{in}}$ , respectively. This spin-dependent behavior of  $G_\sigma$ , which results from the type (i) trajectory of excess charges and the scattering nature of multiple extended edge channels by the antidot (*i.e.*, the sign of  $T_\sigma$ ), is an interesting feature of the antidot Kondo effect.

#### 4.5 Hole maximum-density-droplet antidot ground state

In the previous section, the properties of antidots in the integer quantum Hall regime have been described based on a capacitive interaction model. To have a more solid understanding, it is necessary to go beyond such a phenomenological model by using numerical methods. However, the antidot system is an open-geometry problem and thus may require heavy calculations to treat its interaction effects. The difficulty was avoided in a recent Hartree-Fock study [52] by using a particle-hole transformation. The transformation converts the antidot into a quantum dot of holes. This indicates that one can study an antidot by applying the numerical methods used for a large-size quantum dot.

In the Hartree-Fock calculation in Ref. [52], the properties of the ground state of an antidot containing about 300 holes have been investigated. The main findings of the work are that in a certain parameter range, the ground state of the antidot can be a hole maximum-density droplet, the state without edge reconstruction, and that the transition of the ground states as a function of the magnetic field can be well described by the evolution of the excess charges derived in the capacitive interaction model in Secs. 4.2 and 4.3. This study will be described in this section.

By using a particle-hole transformation [51,98] of the type  $c_{m,\sigma} \rightarrow h_{m,\sigma}^\dagger$  and  $c_{m,\sigma}^\dagger \rightarrow h_{m,\sigma}$ , one can map the  $\nu_c = 2$  antidot system described by the Hamiltonian (28) into a system confining a finite number of holes, for which one can find the eigenstates by using diagonalization. Note that only the lowest Landau levels with the two spin branches are considered for particles and then the particle-hole transformation is performed; the effect of the unoccupied higher Landau levels can be ignored as they provide spatially uniform density of holes and therefore constant energy shift. The transformed total Hamiltonian of holes can have the form [51,52]

$$\begin{aligned}
H &= \sum_{m\sigma}^{m_c} \varepsilon_{m\sigma}^h h_{m\sigma}^\dagger h_{m\sigma} + \frac{1}{2} \sum_{mm'nn'\sigma\sigma'}^{m_c} \langle mm'|W|nn'\rangle h_{n'\sigma'}^\dagger h_{n\sigma}^\dagger h_{m\sigma} h_{m'\sigma'} + E_T, \\
E_T &= 2 \sum_m^{m_c} V_{\text{AD}}(m) - 2 \sum_m^{m_c} W_m^{\text{H}} - \sum_m^{m_c} W_m^{\text{X}}, \\
\varepsilon_{m\sigma}^h &= -V_{\text{AD}}(m) + W_m^{\text{X}} - \epsilon_\sigma^Z,
\end{aligned} \tag{47}$$

$$\varepsilon_{m\sigma}^h = -V_{\text{AD}}(m) + W_m^{\text{X}} - \epsilon_\sigma^Z, \tag{48}$$

where  $\varepsilon_{m\sigma}^h$  is the effective single-particle energy of a hole with angular momentum  $m$ ,  $W_m^{\text{H}} = \sum_{m'}^{m_c} \langle mm'|W|mm'\rangle$ , and  $W_m^{\text{X}} = \sum_{m'}^{m_c} \langle mm'|W|m'm\rangle$ . Here, the angular-momentum wave functions (2) of the lowest Landau level are used as the single-particle basis functions, and  $m_c$  is a cutoff value of angular momentum (chosen sufficiently large). The first term  $V_{\text{AD}}(m) = \langle m|V_{\text{AD}}(r)|m\rangle$  of  $\varepsilon_{m\sigma}^h$  in Eq. (48) means the hole confinement energy coming from the antidot potential  $V_{\text{AD}}$ , while the second term represents the change in exchange energy  $W^{\text{X}}$  when an electron with angular momentum  $m$  disappears; the constant Landau energy  $\hbar\omega_c/2$  is included in  $V_{\text{AD}}(m)$ . A Hartree term  $W^{\text{H}}$  is absent in  $\varepsilon_m$ , since it is canceled by the contribution of the positive background charges. The Zeeman term of  $\varepsilon_{m\sigma}^h$  has the opposite sign to the corresponding term in Eq. (28). The final constant term  $E_T$  of the Hamiltonian  $H$  is the total energy of an electron system in which electrons are occupied from  $m = 1$  to  $m_c$  states. Note that when the cutoff  $m_c$  is much larger than the total number of holes,  $W_m^{\text{X}}$  in Eq. (48) can be treated as a constant [99] so that  $\varepsilon_{m\sigma}^h$  is mainly

governed by  $V_{\text{AD}}(m)$ . In Ref. [52], a bell-shape antidot potential is chosen,

$$V_{\text{AD}}(r) = \begin{cases} \frac{1}{2}\hbar\omega_c - \frac{1}{2}m^*\Omega^2r^2, & r < r_t \\ \frac{1}{2}\hbar\omega_c + \frac{p}{r^2} + q, & r_t < r < r_s \\ \text{constant}, & r > r_s, \end{cases} \quad (49)$$

from which one can easily get the analytic expression for  $V_{\text{AD}}(m)$ . Notice that in the interval  $r < r_t$  the bell-shape potential is inverse parabolic, while in  $r_t < r < r_s$  the curvature changes sign. Here,  $p$  is a parameter determining the curvature in  $r_t < r < r_s$ , while  $q$  is chosen for  $V_{\text{AD}}(r)$  to be continuous at  $r = r_t$ .

The above transformation maps the antidot problem into a numerically tractable finite-size hole system, so that one can study the ground-state properties of an antidot. The properties of the ground state are determined by the competition between the hole confinement potential ( $-V_{\text{AD}}$ ) and the Coulomb energy ( $E^{\text{H}} + E^{\text{X}}$ ). The confinement potential favors a smaller value of total angular momentum of the state. As a result, in the limit of strong hole confinement  $-V_{\text{AD}}(r)$ , the ground state is a maximum-density droplet of holes, which has a single-Slater-determinant form,

$$|N_{\uparrow}^{\text{h}}, N_{\downarrow}^{\text{h}}\rangle = h_{N_{\downarrow}^{\text{h}}-1, \downarrow}^{\dagger} \cdots h_{0, \downarrow}^{\dagger} h_{N_{\uparrow}^{\text{h}}-1, \uparrow}^{\dagger} \cdots h_{0, \uparrow}^{\dagger} |0\rangle. \quad (50)$$

The total number of holes is  $N^{\text{h}} = N_{\uparrow}^{\text{h}} + N_{\downarrow}^{\text{h}}$ , and  $N_{\downarrow}^{\text{h}}$  is equal to or larger than  $N_{\uparrow}^{\text{h}}$  due to the Zeeman energy. The spatial splitting between spin-up and down edges (or  $N_{\downarrow} - N_{\uparrow}$ ) of the droplet depends on the relative strength of the confinement energy and electron-electron interactions; for a given  $N$ , smaller ( $N_{\downarrow}^{\text{h}} - N_{\uparrow}^{\text{h}}$ ) is favored by stronger confinement, since the droplet size is determined by  $N_{\downarrow}^{\text{h}}$ . In Ref. [52], it was found that in certain ranges of system parameters the maximum-density droplet of holes is the ground state of the bell-shaped antidot containing about 300 holes. For weaker confinement, the droplet is not the ground state any more and edge reconstruction such as the formation of compressible regions may occur. Note that an electronic maximum-density droplet has been studied theoretically [99,100] and experimentally [101,102].

Figure 26 shows the transitions between the hole-droplet ground states of the antidot studied in Ref. [52] as a function of  $B$ . The numerical results can be compared with the prediction of the capacitive interaction model in Sec. 4.3. In the parameter regime

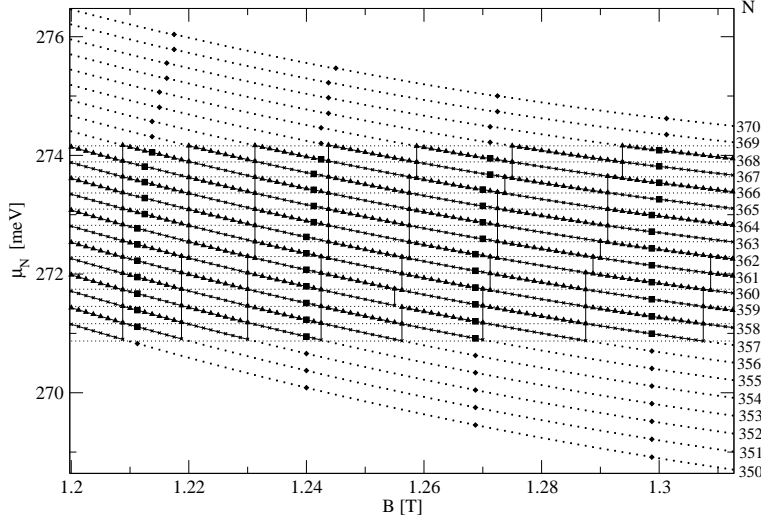


Fig. 26. Chemical potential,  $\mu_{N^h} \equiv E_{N^h+1} - E_{N^h}$ , vs magnetic field  $B$  for a bell-shaped antidot potential. Twenty-one different values of  $N^h = N_{\uparrow}^h + N_{\downarrow}^h \in [350, 370]$  are used. The horizontal dotted line represents the *hole* Fermi energy. Filled squares represent the spin-flip Kondo transitions  $|N_{\uparrow}^h, N_{\downarrow}^h\rangle \rightarrow |N_{\uparrow}^h + 1, N_{\downarrow}^h - 1\rangle$  as  $B$  increases, while vertical jumps show the spin-down resonances  $|N_{\uparrow}^h, N_{\downarrow}^h\rangle \rightarrow |N_{\uparrow}^h, N_{\downarrow}^h + 1\rangle$ . Following the topmost zigzag solid line, for example, the hole maximum-density droplet ground state evolves as  $|N_{\uparrow}^h, N_{\downarrow}^h\rangle = |128, 233\rangle \rightarrow |128, 234\rangle \Rightarrow |129, 233\rangle \rightarrow |129, 234\rangle \rightarrow |129, 235\rangle \Rightarrow |130, 234\rangle \rightarrow |130, 235\rangle \rightarrow |130, 236\rangle \Rightarrow |131, 235\rangle \rightarrow |131, 236\rangle \rightarrow |131, 237\rangle \Rightarrow |132, 236\rangle$  with increasing  $B$ . Similarly, in the fourth zigzag solid line,  $|N_{\uparrow}^h, N_{\downarrow}^h\rangle$  evolves as  $|127, 231\rangle \rightarrow |127, 232\rangle \Rightarrow |128, 231\rangle \rightarrow |128, 232\rangle \rightarrow |128, 233\rangle \Rightarrow |129, 232\rangle \rightarrow |129, 233\rangle \rightarrow |129, 234\rangle \Rightarrow |130, 233\rangle$ . Here  $\rightarrow$  and  $\Rightarrow$  indicate, respectively, the spin-down normal resonance and spin-flip Kondo transitions. The parameters of this antidot can be found in Ref. [52]. From Ref. [52].

studied in Fig. 26, the transitions of the ground state follow the type (i) process with  $\alpha = 1$  (see Fig. 24). Moreover, the transitions are found [52] to be equivalent to those determined by the evolution of the excess charges  $\delta q_{\sigma}(B)/e = N_{\sigma}^{\text{AD}} - a_{\sigma}B - b_{\sigma}$  in Eqs. (37,38) and by the transition conditions (41,42,43); the parameters of the evolution can be uniquely determined as  $a_{\uparrow} = 34.78$  and  $a_{\downarrow} = 54.11$ . This comparison shows that the capacitive-interaction model may work very well for the droplet states.

The droplet studied in Fig. 26 has the following properties. First, the electron interactions between spin-up and down edges of the droplet are very strong, as indicated

by the result of the comparison,  $\alpha = 1$ . Second, since it follows the type (i) process, it can give rise to the  $h/2e$  Aharonov-Bohm oscillations. Third, the studied droplet has spin-dependent areas  $S_\uparrow \neq S_\downarrow$ , as  $N_\uparrow^h \simeq 130$  and  $N_\downarrow^h \simeq 235$ . In this case, only the spin-down electrons may be allowed to tunnel between the droplet and the extended edge channels. Therefore, as discussed in Sec. 4.4, the Kondo effect will be suppressed in this case. To see the Kondo effect, we need  $S_\uparrow \simeq S_\downarrow$ , which can be obtained for a stronger antidot confinement potential than that studied in Fig. 26.

Concluding this section, we note that the Hartree-Fock approach discussed here is valid only when the ground state of the antidot is the hole maximum-density-droplet state. In the next section, we will review a numerical study based on density-functional theory in which the formation of compressible regions around an antidot, another interesting and important type of antidot ground state, can be studied.

#### 4.6 *Density-functional studies on the compressibility of antidot states*

As discussed in Sec. 3.7, it is interesting to study whether compressible regions can be formed around an antidot. Recently, Ihnatsenka and Zozoulenko [60] studied the formation of compressible regions around an antidot numerically by using spin-density-functional theory. They found that screening is less effective in a finite-length antidot edge than in an extended edge with infinite length. This numerical approach will be described in this section.

In the work by Ihnatsenka and Zozoulenko [60], a form of antidot potential (induced from a circular gate of radius 100–500 nm) obtained by Davies [103] was used, and Hartree interactions, exchange correlations, and the effect of Zeeman splitting were taken into account within the framework of density-functional theory in the local spin-density approximation [104]. Compressible regions are defined as the spatial windows in which effective single-particle energy  $E$ , obtained by solving self-consistently a Schrödinger equation within the density-functional theory, satisfies  $|E - E_F| < 2\pi k_B T$ . The features of the compressible regions were studied separately for the spinless and spinful cases in magnetic fields of 1–5 T ( $\nu_c = 2$  is achieved around  $B = 4$  T).

For the spinless case, where the exchange correlations are not taken into account, the calculation shows that the width of the compressible region formed around an antidot becomes narrower, deviating from the value in the extended-edge cases [56,57], as the

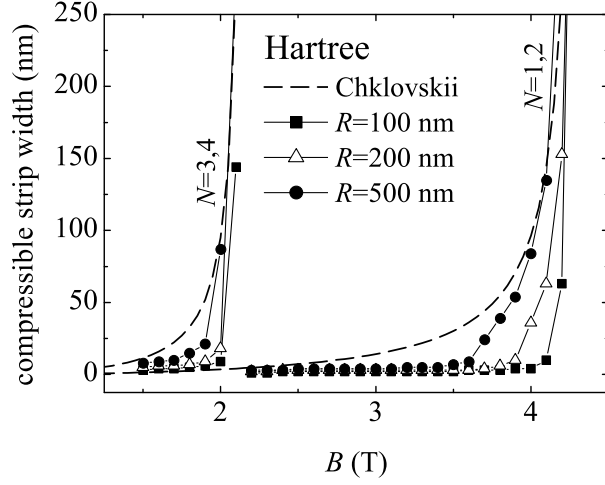


Fig. 27. Width of the compressible regions around an antidot formed by an antidot gate with various radii  $R$  as a function of magnetic field, calculated within the Hartree approximation at temperature  $T = 1$  K for the case of spinless electrons. It is compared with the width of compressible regions formed along extended edge channels calculated by Chklovskii and his coworkers [56,57].  $N = 1,2$  and  $3,4$  refer to the subband number corresponding to the two lowest (spin-degenerate) edge states. From Ref. [60].

radius of the antidot becomes smaller (see Fig. 27). This finding can be understood as follows. Compared with the extended edge cases, the Hartree contribution is stronger in the antidot due to finite-size effects. The stronger Hartree potential repels electrons from the antidot edge, and thus screening properties become weaker, resulting in a steeper effective antidot potential preventing the formation of compressible regions.

For the spinful case, the compressible regions around the antidot show more distinct deviation from the extended edge cases. The contribution from exchange interactions suppresses the formation of the compressible region of spin-up electrons, which is assumed to have lower Zeeman energy than spin down. In the parameter ranges studied in Ref. [60] it was found that the spin-up compressible region is not formed [see Fig. 28(b)]. Moreover, the spin-up and down states at the Fermi level are spatially separated from each other [Figs. 28(c)-(f)]. These results indicate that the edge structure around the antidot could be surprisingly different from that along extended edges due to finite-size effects.

The two numerical studies in this and the previous sections provide useful information on electronic structure around antidots. However, they serve just as a starting point, as they explore only narrow parameter ranges (antidot size, magnetic field, electron

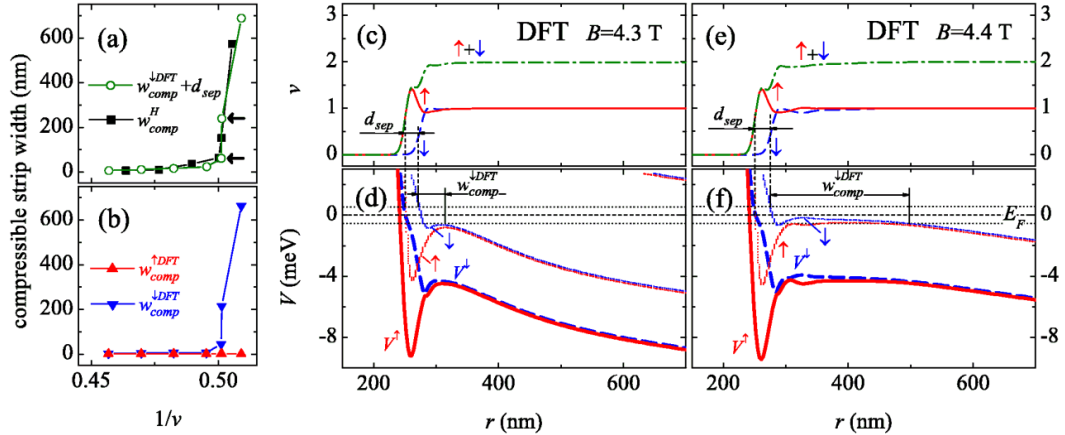


Fig. 28. (a) Width of the compressible regions formed around an antidot for spinless electrons as a function of  $1/\nu$ , where  $\nu$  is the antidot filling factor. The result of a Hartree approximation (filled squares) is almost identical to that calculated using density-functional theory. (b) Width of the compressible regions in the spinful case, calculated using density-functional theory. In the parameter regime studied in this figure, the spin-up compressible region is not formed. (c) and (e) Electron density profiles for different magnetic fields, and (d) and (f) the corresponding magnetosubband structures. From Ref. [60].

density, the smoothness of antidot potential, etc). More systematic numerical studies are required to have the phase diagram which shows when the hole maximum-density droplet, the formation of compressible regions, or any other possible edge reconstruction is the ground state of an antidot. Such studies will be very valuable in order to understand electron interactions in antidots or local disorder regions in the integer quantum Hall regime.

## 5 Summary and perspectives

We have reviewed experimental and theoretical works devoted to electron interactions in an antidot in the integer quantum Hall regime. To conclude this review, we emphasize the usefulness of antidots in future studies. An antidot can be created as an experimentally tunable system like a quantum dot. Therefore, understanding antidot systems will open up a systematic way of studying the nature of electron states in a quantum Hall system, such as localized chiral edge states, quasiparticle tunneling, electron-electron interactions, compressible regions and screening of



electric (Hall) fields, etc. For example, it may provide a useful way of studying local disordered regions in quantum Hall systems, which can be modeled by a combination of antidots and quantum dots [44,45,46,105].

Although, as discussed in this review, many features of antidots have been understood in the past decade, there are still many open questions. Some examples are listed below.

- The phase diagram of the ground state (the hole maximum-density droplet, the formation of compressible regions, or any other possible edge reconstruction) of an antidot has not been studied. Especially, the formation of compressible regions around an antidot is still controversial [24,58,59,60] (see Secs. 3.7 and 4.6).
- It is not understood how the change occurs from a low-magnetic-field regime, with spin-split pairs of states, which can be described by a noninteracting model (see Fig. 6 and its description in Sec. 3.1), to higher-field regimes, where interaction effects such as exchange, charging, and Kondo physics emerge, with separate regions of states for the two spins. The transitions may be sudden or gradual.
- In the regime of strong coupling between antidot states and extended edge channels, where the antidot is not isolated, there is no proper theoretical model describing interaction effects.
- A full description of the spectator mode in antidot molecules is required (see Sec. 3.5).
- Interaction effects in an antidot with filling factor  $\nu_c$  larger than 2 still remain to be investigated in detail experimentally and theoretically.

Future studies in these directions are highly desirable.

In addition, we very briefly note the connection between antidot studies in the integer and fractional quantum Hall regimes. Some of the most interesting aspects of the latter regime are the fractional charge and statistics of quasiparticle excitations. As an antidot can provide an experimentally controllable finite edge of the fractional quantum Hall state, it has been used for studying the fractional excitations. Below, we summarize the previous works on antidots in the fractional regime and discuss possible connection to the studies of the integer regime as well as possible future directions.

- The initial aim of studying an antidot in the fractional regime was to detect the fractional charge of quasiparticles [4,30,31,34,35,106,107] and to measure the energy structure [21]. The ratio of the Aharonov-Bohm periods as a function of the

external magnetic field and a back-gate voltage is related to the change in charge around the antidot in sweeping from one conductance peak to the next, i.e. in moving from one resonance to its neighbor. This charge has been found to be  $\sim e/3$  for  $\nu_c = 1/3$  [4]. It was originally pointed out that such antidot studies of periodicities [4,30,31] are made in equilibrium (on a timescale much longer than the lifetime of quasiparticles), so the system could rearrange during each  $h/e$  or  $e/3$  period on that timescale by methods other than the tunneling of a quasiparticle [30,31]. However, the resonant tunneling that gives rise to a conductance peak is itself measuring the passage of individual particles [in general, at zero bias, resonant tunneling of single charged particles occurs when the many-particle states with and without that charge are degenerate]. This implies that, in conjunction with the above measurement of the difference in trapped charge of these two states [4], the particles do have this measured fractional charge,  $e/3$ , as expected for  $\nu = 1/3$  quasiparticles. Similar measurements imply that the fractional charge of quasiparticles in the  $2/5$  state is  $e/5$  [106]. Shot-noise measurements [108,109], performed out of equilibrium using a quantum point contact, have also measured fractional charge.

- In the fractional regime, the antidot state can be described by a chiral Luttinger liquid. Its Hamiltonian has a similar form to the Hamiltonian of the integer regime; see Eq. (33) of Sec. 4.2. It has been suggested [36,37] that an antidot can be used to distinguish experimentally between Luttinger and Fermi liquids, as the Aharonov-Bohm oscillations can show the crossover between them. The crossover remains to be tested experimentally [32]. It has been also investigated [38], based on the chiral Luttinger-liquid theory, that the statistics of quasiparticle tunneling in an antidot system can reveal its features in high moments of the tunneling current. These theoretical works suggest that the antidot can provide an experimental system for studying a finite-size Luttinger liquid.
- We have seen that the many-body ground state of an antidot and the reconstruction of the antidot edge are important issues in the integer regime (see Secs. 3.7 and 4.6). The edge reconstruction is also important in the fractional regime as it is determined by the interplay of electron-electron interaction in the fractional regime, the single-particle electrostatic edge potential (or antidot potential), and effects of finite temperature. A recent numerical prediction [110] on edge reconstruction in the fractional regime has been linked to experimental results [111] on the microwave conductivity of two-dimensional electron systems with an array of antidots. More systematic studies on the edge reconstruction are required to understand excitations of an antidot in both the integer and fractional regimes.
- An antidot molecule has been also studied [33] in the fractional regime, focusing

on coherent tunneling between two antidot bound states (for the integer regime, see Sec. 3.5). In the antidot studied, the coherent tunneling rate between the two bound states was found to be an order of magnitude higher than the phase-breaking rate. Coulomb blockade of an antidot molecule has been theoretically studied very recently as well [112]. These works may be a starting point for implementing quantum computation using antidots [113,114].

- It has been suggested [39,40] to use antidots for detecting non-Abelian braiding statistics of the Pfaffian state [115,116] in the  $\nu = 5/2$  regime. An experimental test of this proposal is still needed, and such a test would provide a way of constructing topologically protected qubits based on a non-Abelian fractional state.

Finally, we would like to point out that antidots can provide various powerful experimental tools. For example, they can be used to study departures from the Onsager relations in nonlinear mesoscopic transport [117], and can constitute a spin injector or spin filter [118], which may be useful for spintronics using quantum-Hall edge channels.

## Acknowledgements

We are grateful to L. C. Bassett for critical reading and useful discussions. We also thank V. J. Goldman, A. S. Sachrajda, and I. V. Zozoulenko for providing their figures and for valuable comments. We are supported by a Korean Research Foundation Grant funded by the Korean Government (KRF-2006-331-C00118, KRF-2005-070-C00055), and by the UK EPSRC.

## References

- [1] C. J. B. Ford, P. J. Simpson, I. Zailer, D. R. Mace, M. Yosefin, M. Pepper, D. A. Ritchie, J. E. F. Frost, M. P. Grimshaw, G. A. C. Jones, Phys. Rev. B 49 (1994) 17456.
- [2] A. S. Sachrajda, Y. Feng, R. P. Taylor, G. Kirczenow, L. Henning, J. Wang, P. Zawadzki, P. T. Coleridge, Phys. Rev. B 50 (1994) 10856.
- [3] S. W. Hwang, J. A. Simmons, D. C. Tsui, M. Shayegan, Phys. Rev. B 44 (1991) 13497.
- [4] V. J. Goldman, B. Su, Science 267 (1995) 1010.

- [5] H. Grabert, M. H. Devoret, *Single Charge Tunneling: Coulomb Blockade Phenomena in Nanostructures*, Plenum Press, 1992.
- [6] L. L. Sohn, L. P. Kouwenhoven, G. Schön, *Mesoscopic Electron Transport*, Kluwer Academic Publishers, 1997.
- [7] J. K. Jain, S. A. Kivelson, *Phys. Rev. Lett.* 60 (1988) 1542.
- [8] G. Timp, A. M. Chang, P. Mankiewich, R. Behringer, J. E. Cunningham, T. Y. Chang, R. E. Howard, *Phys. Rev. Lett.* 59 (1987) 732.
- [9] C. G. Smith, M. Pepper, R. Newbury, H. Ahmed, D. G. Hasko, D. C. Peacock, J. E. F. Frost, D. A. Ritchie, G. A. C. Jones, G. Hill, *J. Phys.: Cond. Mat.* 1 (1989) 6763.
- [10] D. Weiss, M. L. Roukes, A. Menschig, P. Grambow, K. von Klitzing, G. Weimann, *Phys. Rev. Lett.* 66 (1991) 2790.
- [11] W. Kang, H. L. Stormer, L. N. Pfeiffer, K. W. Baldwin, K. W. West, *Phys. Rev. Lett.* 71 (1993) 3850.
- [12] J. H. Smet, K. von Klitzing, D. Weiss, W. Wegscheider, *Phys. Rev. Lett.* 80 (1998) 4538.
- [13] R. Fleischmann, T. Geisel, R. Ketzmerick, *Phys. Rev. Lett.* 68 (1992) 1367.
- [14] D. Weiss, K. Richter, A. Menschig, R. Bergmann, H. Schweizer, K. von Klitzing, G. Weimann, *Phys. Rev. Lett.* 70 (1993) 4118.
- [15] T. Chakraborty, P. Pietiläinen, *The Quantum Hall Effects: Integral and Fractional*, Springer, 1995.
- [16] B. I. Halperin, *Phys. Rev. B* 25 (1982) 2185.
- [17] G. Kirczenow, A. S. Sachrajda, Y. Feng, R. P. Taylor, L. Henning, J. Wang, P. Zawadzki, P. T. Coleridge, *Phys. Rev. Lett.* 72 (1994) 2069.
- [18] D. R. Mace, C. H. W. Barnes, G. Faini, D. Maily, M. Y. Simmons, C. J. B. Ford, M. Pepper, *Phys. Rev. B* 52 (1995) R8672.
- [19] C. H. W. Barnes, D. R. Mace, G. Faini, D. Maily, M. Y. Simmons, C. J. B. Ford and M. Pepper, *Surf. Sci.* 362 (1996) 608.
- [20] G. Kirczenow, B. L. Johnson, P. J. Kelly, C. Gould, A. S. Sachrajda, Y. Feng, A. Delage, *Phys. Rev. B* 56 (1997) 7503.
- [21] I. J. Maasilta, V. J. Goldman, *Phys. Rev. B* 57 (1998) R4273.

- [22] M. Kataoka, C. J. B. Ford, G. Faini, D. Maily, M. Y. Simmons, D. R. Mace, C.-T. Liang, D. A. Ritchie, *Phys. Rev. Lett.* 83 (1999) 160.
- [23] M. Kataoka, C. J. B. Ford, G. Faini, D. Maily, M. Y. Simmons, D. A. Ritchie, *Phys. Rev. B* 62 (2000) R4817.
- [24] I. Karakurt, V. J. Goldman, J. Liu, A. Zaslavsky, *Phys. Rev. Lett.* 87 (2001) 146801.
- [25] M. Kataoka, C. J. B. Ford, M. Y. Simmons, D. A. Ritchie, *Phys. Rev. Lett.* 89 (2002) 226803.
- [26] M. Kataoka, C. J. B. Ford, M. Y. Simmons, D. A. Ritchie, *Phys. Rev. B* 68 (2003) 153305.
- [27] C. Gould, A. S. Sachrajda, Y. Feng, A. Delage, P. J. Kelly, K. Leung, P. T. Coleridge, *Phys. Rev. B* 51 (1995) 11213.
- [28] C. Gould, A. S. Sachrajda, M. W. C. Dharma-wardana, Y. Feng, P. T. Coleridge, *Phys. Rev. Lett.* 77 (1996) 5272.
- [29] G. Kirczenow, B. L. Johnson, P. J. Kelly, C. Gould, A. S. Sachrajda, Y. Feng, A. Delage, *Phys. Rev. B* 56 (1997) 7503.
- [30] C. J. B. Ford, P. J. Simpson, I. Zailer, J. D. F. Franklin, C. H. W. Barnes, J. E. F. Frost, D. A. Ritchie and M. Pepper, *J. Phys.: Condens. Matt.* 6 (1994) L725.
- [31] J.D.F. Franklin, I. Zailer, C. J. B. Ford, P. J. Simpson, J. E. F. Frost, D. A. Ritchie, M. Y. Simmons and M. Pepper, *Surface Science*, 362 (1996) 17.
- [32] I. J. Maasilta, V. J. Goldman, *Phys. Rev. B* 55 (1997) 4081.
- [33] I. J. Maasilta, V. J. Goldman, *Phys. Rev. Lett.* 84 (2000) 1776.
- [34] V. J. Goldman, I. Karakurt, J. Liu, and A. Zaslavsky, *Phys. Rev. B* 64 (2001) 085319.
- [35] V. J. Goldman, J. Liu, A. Zaslavsky, *Phys. Rev. B* 71 (2005) 153303.
- [36] M. R. Geller, D. Loss, G. Kirczenow, *Phys. Rev. Lett.* 77 (1996) 5110.
- [37] M. R. Geller and D. Loss, *Phys. Rev. B* 56 (1997) 9692.
- [38] A. Braggio, N. Magnoli, M. Merlo, M. Sasseti, *Phys. Rev. B* 74 (2006) 041304(R).
- [39] P. Bonderson, A. Kitaev, and K. Shtengel, *Phys. Rev. Lett.* 96 (2006) 016803.
- [40] A. Stern and B. I. Halperin, *Phys. Rev. Lett.* 96, (2006) 016802.
- [41] S. Das Sarma, M. Freedman, and C. Nayak, *Phys. Rev. Lett.* 94 (2005) 166802.

- [42] Y. Takagaki, D. K. Ferry, Phys. Rev. B 48 (1993) 8152.
- [43] G. Kirczenow, Phys. Rev. B 50 (1994) 1649.
- [44] N. B. Zhitenev, T. A. Fulton, A. Yacoby, H. F. Hess, L. N. Pfeiffer, K. W. West, Nature 404 (2002) 473.
- [45] G. Finkelstein, P. I. Glicofridis, R. C. Ashoori, M. Shayegan, Science 289 (2002) 91.
- [46] S. Ilani, J. Martin, E. Teitelbaum, J. H. Smet, D. Mahalu, V. Umansky, A. Yacoby, Nature 427 (2004) 328.
- [47] Y. Ji, Y. Chung, D. Sprinzak, M. Heiblum, D. Mahalu, H. Shtrikman, Nature 422 (2003) 415.
- [48] I. Neder, M. Heiblum, Y. Levinson, D. Mahalu, V. Umansky, Phys. Rev. Lett. 96 (2006) 016804.
- [49] H.-S. Sim, M. Kataoka, Hangmo Yi, N. Y. Hwang, M.-S. Choi, S.-R. E. Yang, Phys. Rev. Lett. 91 (2003) 266801.
- [50] L. I. Glazman, M. Pustilnik, cond-mat/0302159.
- [51] H.-S. Sim, N. Y. Hwang, M. Kataoka, Hangmo Yi, M.-S. Choi, S.-R. E. Yang, Physica E 22 (2004) 554.
- [52] N. Y. Hwang, S.-R. E. Yang, H.-S. Sim, Hangmo Yi, Phys. Rev. B 70 (2004) 085322.
- [53] S.-R. E. Yang, N. Y. Hwang, H.-S. Sim, Hangmo Yi, Int. J. Mod. Phys. B 18 (2004) 3657.
- [54] C. W. J. Beenakker, Phys. Rev. Lett. 64 (1990) 216.
- [55] A. M. Chang, Solid State Commun. 74 (1990) 871.
- [56] D. B. Chklovskii, B. I. Shklovskii, L. I. Glazman, Phys. Rev. B 46 (1992) 4026.
- [57] D. B. Chklovskii, K. A. Matveev, B. I. Shklovskii, Phys. Rev. B 47 (1993) 12605.
- [58] M. Kataoka, C. J. B. Ford, Phys. Rev. Lett. 92 (2004) 199703.
- [59] V. J. Goldman, Phys. Rev. Lett. 92 (2004) 199704.
- [60] S. Ihnatsenka, I. V. Zozoulenko, Phys. Rev. B 74 (2006) 201303(R).
- [61] C. P. Michael, M. Kataoka, C. J. B. Ford, G. Faini, D. Mailly, M. Y. Simmons and D. A. Ritchie, Physica E, 34 (2006) 195.

- [62] T. K. Ng, P. A. Lee, Phys. Rev. Lett. 61 (1988) 1768.
- [63] M. Büttiker, Phys. Rev. Lett. 57 (1986) 1761.
- [64] M. Kataoka, *et al. unpublished*.
- [65] M. Field, C. G. Smith, M. Pepper, D. A. Ritchie, J. E. F. Frost, G. A. C. Jones, D. G. Hasko, Phys. Rev. Lett. 70 (1993) 1311.
- [66] R. P. Taylor, A. S. Sachrajda, P. Zawadzki, P. T. Coleridge, J. A. Adams, Phys. Rev. Lett. 69 (1992) 1989.
- [67] B. W. Alphenaar, A. A. M. Staring, H. van Houten, M. A. A. Mabeesoone, C. T. Foxon, Phys. Rev. B 46, (1992) 7236.
- [68] A. S. Sachrajda, R. P. Taylor, C. Dharma-Wardans, P. Zawadzki, J. A. Adams, P. T. Coleridge, Phys. Rev. B 47 (1992) 6811.
- [69] A. A. M. Staring, B. W. Alphenaar, H. van Houten, L. W. Molenkamp, O. J. A. Buyk, M. A. A. Mabeesoone, C. T. Foxon, Phys. Rev. B 46 (1992) 12869.
- [70] M. W. C. Dharma-Wardana, R. P. Taylor, A. S. Sachrajda, Solid State Commun. 84 (1992) 631.
- [71] A. Sachrajda, R. P. Taylor, C. Dharma-wardana, J. A. Adams, P. Zawadzki and P. T. Coleridge, Surf. Sci. 305 (1994) 527.
- [72] B. J. van Wees, E. M. M. Willems, C. J. P. M. Harmans, C. W. J. Beenakker, H. van Houten, J. G. Williamson, C. T. Foxon, J. J. Harris, Phys. Rev. Lett. 62 (1989) 1181.
- [73] G. Müller, D. Weiss, A. V. Khaetskii, K. von Klitzing, S. Koch, H. Nickel, W. Schlapp, R. Lösch, Phys. Rev. B 45 (1992) 3932.
- [74] Y. Takagaki, Phys. Rev. B 55 (1997) R16021.
- [75] D. V. Averin, K. K. Likharev, in Mesoscopic Phenomena in Solids, Elsevier, Amsterdam, 1991.
- [76] L. I. Glazman, R. I. Shekhter, J. Phys.: Cond. Mat. 1 (1989) 5811.
- [77] C. W. J. Beenakker, Phys. Rev. B 44 (1991) 1646.
- [78] Y. Y. Wei, J. Weis, K. v. Klitzing, K. Eberl, Phys. Rev. Lett. 81 (1998) 1674.
- [79] K. Lier, R. R. Gerhardts, Phys. Rev. B 50 (1994) 7757.
- [80] L. C. Bassett, C. P. Michael, C. J. B. Ford, M. Kataoka, C. H. W. Barnes, M. Y. Simmons and D. A. Ritchie, *to be published*.

- [81] J. Kondo, *Prog. Theor. Phys.* 32 (1964) 37.
- [82] A. C. Hewson, *The Kondo Problem to Heavy Fermions*, Cambridge University Press, Cambridge, 1993.
- [83] L. I. Glazman, M. E. Raikh, *JETP Lett.* 47 (1988) 452.
- [84] D. Goldhaber-Gordon, H. Shtrikman, D. Mahalu, D. Abusch-Magder, U. Meirav, M. A. Kastner, *Nature* 391 (1998) 156.
- [85] S. M. Cronenwett, T. H. Oosterkamp, L. P. Kouwenhoven, *Science* 281 (1998) 540.
- [86] W. G. van der Wiel, S. De Franceschi, T. Fujisawa, J. M. Elzerman, S. Tarucha, L. P. Kouwenhoven, *Science* 289 (2000) 2105.
- [87] D. Goldhaber-Gordon, J. Göres, M. A. Kastner, H. Shtrikman, D. Mahalu, U. Meirav, *Phys. Rev. Lett.* 81 (1998) 5225.
- [88] M. Keller, Y. Wilhelm, J. Schmid, J. Weis, K. v. Klitzing, K. Eberl, *Phys. Rev. B* 64 (2001) 033302.
- [89] D. J. Thouless, Y. Gefen, *Phys. Rev. Lett.* 66 (1991) 806.
- [90] T. Inoshita, A. Shimizu, Y. Kuramoto, H. Sakaki, *Phys. Rev. B* 48 (1993) 14725.
- [91] D. Boese, W. Hofstetter, H. Schoeller, *Phys. Rev. B* 66 (2002) 125315.
- [92] Y. Meir, N. S. Wingreen, P. A. Lee, *Phys. Rev. Lett.* 70 (1993) 2601.
- [93] K. G. Wilson, *Rev. Mod. Phys.* 47 (1975) 773.
- [94] T. A. Costi, A. C. Hewson, V. Zlatic, *J. Phys.: Cond. Mat.* 6 (1994) 2519.
- [95] R. López, D. Sánchez, *Phys. Rev. Lett.* 90 (2003) 116602.
- [96] J. Martinek, Y. Utsumi, H. Imamura, J. Barnas, S. Maekawa, J. König, G. Schön, *Phys. Rev. Lett.* 91 (2003) 127203.
- [97] F. D. M. Haldane, *Phys. Rev. Lett.* 40 (1978) 416.
- [98] M. D. Johnson, A. H. MacDonald, *Phys. Rev. Lett.* 67 (1991) 2060.
- [99] A. H. MacDonald, S.-R. Eric Yang, M. D. Johnson, *Aust. J. Phys.* 46 (1993) 345.
- [100] S.-R. Eric Yang, A. H. MacDonald, M. D. Johnson, *Phys. Rev. Lett.* 71 (1993) 3194.
- [101] O. Klein, C. de C. Chamon, D. Tang, D. M. Abusch-Magder, U. Meirav, X.-G. Wen, M. A. Kastner, *Phys. Rev. Lett.* 74 (1995) 785.



- [102] T. H. Oosterkamp, J. W. Janssen, L. P. Kouwenhoven, D. G. Austing, T. Honda, S. Tarucha, *Phys. Rev. Lett.* 82 (1999) 2931.
- [103] J. H. Davies, *Semicond. Sci. Technol.* 3 (1988) 995.
- [104] R. G. Parr, W. Yang, *Density-Functional Theory of Atoms and Molecules*, Oxford Science, Oxford, 1989.
- [105] D. H. Cobden, C. H. W. Barnes, and C. J. B. Ford, *Phys. Rev. Lett.* 82 (1999) 4695-4698.
- [106] V. J. Goldman, *Surf. Sci.* 263 (1996) 1.
- [107] V. J. Goldman, *Physica E* 1 (1997) 15.
- [108] R. de-Picciotto, M. Reznikov, M. Heiblum, V. Umansky, G. Bunin and D. Mahalu, *Nature* 389 (1997) 162.
- [109] L. Saminadayar, D. C. Glattli, Y. Jin and B. Etienne, *Phys. Rev. Lett.* 79 (1997) 2526.
- [110] X. Wan, K. Yang, and E. H. Rezayi, *Phys. Rev. Lett.* 88 (2002) 056802.
- [111] P. D. Ye, L. W. Engel, D. C. Tsui, J. A. Simmons, J. R. Wendt, G. A. Vawter, and J. L. Reno, *Phys. Rev. B* 65 (2002) 121305(R).
- [112] D. V. Averin and J. A. Nesteroff, *Phys. Rev. Lett.* 99 (2007) 096801.
- [113] D. V. Averin and V. J. Goldman, *Solid State Commun.* 121 (2002) 25.
- [114] F. E. Camino, W. Zhou, and V. J. Goldman, *Phys. Rev. B* 74 (2006) 115301.
- [115] G. Moore and N. Read, *Nucl. Phys. B* 360 (1991) 362.
- [116] M. Greiter, X. G. Wen, and F. Wilczek, *Nucl. Phys. B* 374 (1992) 567.
- [117] D. Sánchez, M. Büttiker, *Phys. Rev. Lett.* 93 (2004) 106802.
- [118] I. V. Zozoulenko, M. Evaldsson, *Appl. Phys. Lett.* 85 (2004) 3136.